MECHANICAL CHARACTERIZATION AND THERMAL MODELING OF A MEMS THERMAL SWITCH

By

KEVIN RICHARD CRAIN

A thesis submitted in partial fulfillment of
the requirements for the degree of

MASTER OF SCIENCE IN MECHANICAL ENGINEERING

WASHINGTON STATE UNIVERSITY
School of Mechanical and Materials Engineering

December 2005

To the Faculty of Washington State University:

The members of the Committee appointed to examine the thesis of KEVIN RICHARD CRAIN find it satisfactory and recommend that it be accepted.

_____
Chair

_____

_____

ACKNOWLEDGEMENTS

This research would not be possible without the patient help and guidance of my advisor, Dr. Bob Richards. His involvement and support has made this research successful. From him I have gained wisdom and knowledge that will carry me into a career that I know will continue with the success that began here with my graduate studies. From my other committee members, Dr. Cill Richards and Dr. Dave Bahr, I have gained new insight into research and engineering. Their knowledge and expertise in a variety of areas has been invaluable to me in my pursuits in graduate school, and I will carry that knowledge with me throughout my career.

I also acknowledge the entire P3 MEMS group for their hard work and dedication to an extraordinary research project. Their example and never-die attitude is what makes this research project successful. I specifically want to thank Jeong-Hyun Cho for his help and advice regarding thermal switch fabrication, Leland Weiss for advice, suggestions, and help regarding experimentation, and Aireus Christensen and Travis Wiser for their work as fellow thermal switch researchers.

I thank all my friends and family for their support and encouragement as I progressed through this challenging period of my life. I especially thank my wife Cristin, who stood by me during struggles and rejoiced with me in success. Finally, I thank God for blessing me and guiding me through until the end.

MECHANICAL CHARACTERIZATION AND THERMAL MODELING OF A MEMS THERMAL SWITCH

Abstract

by Kevin Richard Crain, M.S.
Washington State University
December 2005

Chair: Robert Richards

This thesis summarizes the research involved in mechanically characterizing a liquid metal micro droplet array thermal switch for use with the P3 micro heat engine under development at Washington State University. The mechanical characterization of the thermal switch was completed with the development of a thermal model that predicts the thermal resistance of the droplet array when in contact with the P3 engine at various loadings.

The thermal switch was mechanically characterized statically, dynamically, as well as statistically. Static deformation experiments of single large droplets of 200μm diameters provided a means for validating the mechanical and geometrical aspects of the thermal model, such as force, deflection, and contact diameter. Deflection and contact diameter were measured simultaneously under static conditions with applied forces ranging from 0 to 0.1N. Dynamic droplet array behavior was experimentally observed by visualizing cyclic actuation of the droplet arrays against a rigid, glass surface. Actuation frequencies of 20Hz and 400 Hz were applied to the droplet arrays using a piezoelectric actuator stack, over varying lengths of actuation time, for total cycle spans of one, ten, and one hundred thousand cycles, as well as one million cycles. Statistical

characterization was obtained using computer-assisted droplet diameter measurement of digital photographs of the droplet arrays. Total array population was also statistically inferred from sample population data analysis.

Analytical models were derived for geometry, mechanical deformation, and thermal behavior. Geometrical relationships between contact radius and deformed droplet height were derived, assuming constant volume and contact angle of the liquid/solid/vapor interface. This was converted into contact diameter and deflection for comparison and validation with experimental measurements. Experimental mechanical deformation data was compared and validated against a model based on capillary pressure of the liquid droplet. This model was used to obtain a corresponding relationship between force and deflection of a deformed droplet. These models were then incorporated into a thermal model which calculates an effective thermal resistance for a network of resistances of the droplets and gas gaps in the array. The geometric and force models were used to calculate the theoretical thermal resistance of every droplet in an array under a specific loading. Forces between 0 and 1N were used to calculate the thermal resistance of a droplet array. Different interstitial gas environments of air, vacuum, and xenon, were applied to the thermal model to investigate possible increases in performance of the droplet arrays.

TABLE OF CONTENTS

LIST OF TABLES

LIST OF FIGURES

CHAPTER 1

INTRODUCTION

1.1 Motivation

Micromechanical switches are finding applications in thermal MEMS research, which include thermopneumatic actuators and micro heat engines. A novel external combustion micro heat engine is being developed at Washington State University (WSU) [1,2], which requires the use of a thermal switch to conduct heat into and out of the engine. The thermal switch must function at the resonant frequency of the engine and be able to transfer appropriate amounts of heat into and out of the engine at particular times, in order for the engine to run as efficiently as possible. The motivation of this research is to develop a thermal model that will predict the performance of a thermal switch to be used in conjunction with the P3 micro heat engine under development at WSU. The ultimate goal is to design more efficient thermal switches that will increase engine performance.

1.2 Literature Review

Thermal switches, also known as heat switches, are a popular area of research. The scope of thermal switch applications is broad and diverse. However, the consistent need in industry centers on thermal control. Two applications of thermal switches involve the areas of space exploration and cryogenics. A third application includes biomedical DNA replication (also known as polymerase chain reaction, or PCR). Other applications of micromechanically designed thermal switches that are increasing in popularity and importance include low temperature physics, solid state thermoelectric

coolers, and micro heat engines. These applications will be discussed in greater detail to provide conceptual understanding of the need for thermal switches.

In thermal switch design, thermal resistance (or inversely, thermal conductance) is the principle parameter of interest. In designing an effective thermal switch, thermal resistance should be minimized when the thermal switch is activated, allowing the maximum quantity of heat to transfer across the switch. When the thermal switch is deactivated, thermal resistance should be maximized in order to minimize heat transfer and conserve energy. Contact resistance is also an integral part of thermal resistance and must be considered when designing thermal switches. Several aspects of thermal switch design will be discussed below.

Characterizing thermal switch behavior is also important. A thermal switch controls the flow of heat in a mechanical system. This is analogous to controlling electric current in electrical systems, such as an electrical switch for a light fixture in a house. At times, the light must be turned on to illuminate a room. When there is no longer a need for illumination, turning the light off will conserve electricity. In similar fashion, some mechanical systems require heat transfer during a specific, finite period of time. When the thermal switch is activated, or turned on, heat is transferred across the switch as the thermal resistance is minimized. When heat transfer is no longer required, the thermal switch is deactivated, thereby increasing thermal resistance and minimizing heat transfer across the thermal switch. Characterizing the behavior of thermal switches is imperative to ensure functional performance of the design and application of a thermal switch. For the thermal switch application and design involved in this research, theoretical characterization of expected performance will also be discussed.

1.2.1 Thermal Switch Applications

There is great interest in the ability to control heat flow in mechanical systems. Space applications have traditionally been one of the most important areas for thermal switching. In particular, thermal switches have been applied to the area of cryogenics for spacecraft. Spacecraft radiation sensors, such as infrared and gamma ray detectors [3], need to function at extremely low temperatures. Thermal switches are used to couple these sensors to cryogenic refrigerators. When the sensor is operating, the thermal switch is activated to dissipate heat produced by the sensor through the switch to the refrigerator. When not operating, the sensor is disconnected from the refrigerator. Likewise, parasitic heat loads from refrigerators in redundant cooling systems can be disconnected using thermal switches. The thermal switch is deactivated to provide high thermal resistance to isolate the sensor [4].

Other reasons for decoupling the sensor from the cryogenic cooler include cases of open cycle systems that use expendable cryogens as coolant. Conservation of the expendable coolants increases the lifespan of the system and elongates the mission duration capability of the device. In addition, decoupling the sensor from the cooler reduces contaminants that collect on the sensor during cryogenic operation. Often these contaminants can be removed by the resulting gradual warm up during inactivity [3].

Another application is thermal control of spacecraft via radiative heat transfer between the craft and the environment. The traditional approach to spacecraft thermal control involves large radiators connected to louver structures controlled by a thermostat [5]. However, in applications where satellites are very small (weighing less than 20 kg, known as nanosats or picosats), this approach is difficult. Possible alternatives include

variable emissivity coatings (VEC) that can actively control heat transfer from the spacecraft in response to variations in thermal load and radiative conditions. Along these lines, one promising option is the active radiator tile (ART) thermal valve, a new form of MEMS thermal switch [6].

The areas of research for thermal switch integration include low temperature calorimetry [7], nuclear demagnetization cryostats [8], adiabatic demagnetization [9], and Pomeranchuk cooling (which is solidification of liquid helium via adiabatic compression) [9]. In low temperature calorimetry, a sample is cooled with a refrigerator and then isolated using a thermal switch. The measurement then proceeds by applying a controlled heat pulse and observing the associated temperature rise. Adiabatic demagnetization requires precooling the paramagnet and additional materials in a magnetic field by a refrigerator. The thermal switch then isolates the specimens and the magnetic field is lowered adiabatically to zero [9].

Solid state cooler applications, such as thermoelectrics (TE's), have benefited from thermal switches. TE's have advantages of high reliability, low mechanical noise, and localized temperature control. However, they typically have low efficiency and frequently need multiple stages to be effective. In order to make solid state cooling competitive, implementation of thermal switches in the transient operation of thermoelectric coolers has been achieved. Application of short transient pulses on top of a steady state bias results in an additional temperature drop over the performance of steady state TE cooling [10]. Sensors, detectors, and signal processing perform better in reduced temperature environments. Solid state coolers enable the system designer to

tightly control the device temperature to specific ranges over varying power dissipation levels by using active sensing and feedback [10].

Biomedical research may appear unrelated to applications of a thermal switch, but polymerase chain reaction (PCR) is an area in which carefully controlled heat transfer is crucial. PCR is a process through which DNA is replicated millions of times. It is a process that is mediated by enzymes and consists of periodic repetition of three biological reaction steps which each occur at different temperatures. The basic requirement for efficient DNA amplification is rapid heat transfer [11]. A device with low heat capacity and high thermal conductivity is desired for optimal PCR. With traditional PCR instruments, heating and cooling rates are slow, due to the relatively large size of thermal components. Pulsed resistance heaters have been successfully used in microchip PCR devices [11], but thermal switches could potentially be used in these applications as an alternative to resistance heaters. MEMS-based thermal switches, with naturally higher surface area to volume ratios, may produce faster heat transfer rates and thus could accelerate the PCR amplification process. At this time, implementation of a MEMS thermal switch has not occurred, but the characteristics of thermal switches suggest possible benefits could be gained from application of thermal switches in PCR.

1.2.2 Thermal Switch Designs

There have been several thermal switch designs applied to the requirements of space-based cryogenic systems [3, 4, 12]. A gas-gap thermal switch consists of two cylindrical pieces that are separated by a small gap filled with a conductive gas. The thermal resistance varies with respect to the amount of gas that fills the gap. Reported methods of pumping the gas into the cylinders have utilized cryogenic and charcoal

pumps. Actuation times are dependent on allowing the gap to fill with gas, and they are on the order of minutes, making these thermal switches very slow. However, thermal resistance ratios have been reported as high as 1500 [3] and 4000 [12]. Another thermal switch design revolves around the differential thermal expansion of distinct metals [4]. Actuation times are dependent on the materials used.

The difference between the gas gap and dissimilar metal switch designs is the method of actuation. The former is actively actuated, requiring external energy to operate. The latter is passively actuated as a function of the mean temperature of the switch. Other thermal switches include solenoid-activated, metal to metal contact switches. Single gallium crystal switches operate at temperatures of liquid helium and are switched by magnetic fields. Heat pipes have also been used as thermal switches and operate relative to the delay times that allow the nitrogen working fluid to transfer along the length of the pipe [4].

The ART (active radiator tile) thermal switch utilizes electrostatic actuation to control the thermal switch [6]. The ART is comprised of two material layers, separated by an evacuated gap. Thus, the two layers, the external radiator and the internal base plate, are thermally isolated. Inside the gap, the two opposing surfaces are coated with a low emissivity material to minimize radiation across the gap. The external surface of the tile is coated with a high emissivity coating to maximize the radiative heat transfer into space. The external radiator is fabricated out of silicon, which has high thermal conductivity. A large membrane with a central contacting mass is etched into the silicon. When an electrostatic charge is applied to the ART, the membrane deflects into intimate, mechanical contact with the hot base plate. Heat is then conducted to the radiator and

radiated to the environment. The temperature differential across the 10μm gap in the switch was reported as high as 145°C in the off state. The thermal resistance of the ART was not reported.

Spacecraft are not the only area of development for thermal switch integration. The field of low temperature physics frequently employs exotic thermal switch designs, such as superconducting [7, 8, 13] and cryogenic [9, 14] thermal switches, in research.

Superconducting thermal switches "rely on the fact that the thermal conductivity of a superconducting material in the normal state is substantially larger than its conductivity in the superconducting state [7]." Some superconducting materials used in thermal switches include indium, aluminum, tin, lead, zinc [7], as well as cold-pressed Cu-Al composites [8].

One cryogenic thermal switch relies on the thermal properties of liquid helium which can achieve a thermal conductance similar to electrolytic copper [14]. Actuation is done using a self contained cryopump. Heating the cryopump to a temperature where the helium is desorbed activates the thermal switch, and cooling the cryopump reabsorbs the helium. The reported ratio of on and off conductance was greater than 10^4 with switching times on the order of minutes.

1.2.3 Thermal Contact Resistance

Contact resistance is an important factor to consider when discussing thermal switches. Contact resistance arises from a non-ideal contact at the interface between two solid surfaces that are brought into contact. The purpose of this contact is typically for transferring heat or electricity from one body to another through conduction. When the surfaces are in contact, the real contact area is only a fraction of the apparent contact area

due to asperities and roughness of the two contacting surfaces. An interstitial medium or vacuum occupies the remaining space between the surfaces and this creates a resistance to heat or electricity transfer.

Quantifying this contact resistance can be a complicated process and is frequently inaccurate. These contact resistances can be small, yet quite significant when highly accurate measurements must be made. The magnitude of the contact resistance is a function of the force applied at the interface between the two contacting bodies. As more force is applied, the pressure at the interface increases and the gaps between the two bodies shrinks that produces a lower thermal resistance of the gap. Much work has been done to characterize the behavior of contact resistance, with respect to loading conditions, temperatures, and different material interfaces [15]. Thermal contact conductance of copper contacts was measured over a range of contact pressures of 1 to over 10 MPa, with corresponding thermal contact conductances ranging from 5 to 130 kW/m^2K, respectively. Obviously, the pressure at the interface has a significant influence on the conductivity, or inversely the resistance, of the contact.

Thermal contact resistance has proved to be important in cryogenic engineering. Cryogenically cooled superconducting magnets use high temperature superconductors as power current leads. It is frequently necessary to electrically connect the high temperature superconductors with copper leads, and the thermal contact resistance between these two materials is crucial to understand for proper operation [16]. The contact resistance was measured for superconducting polycrystals connected to copper leads for a variety of connection methods and over a temperature range of 10 to 200K.

The thermal contact resistivity results varied widely between 10^1 and 10^4 mm^2K/W throughout the temperature range.

In this research, thin gold layers are used as condensation targets for the mercury vapor. At the interface between the silicon dioxide and the gold thin film, potential contact resistances exist. To optimize thermal switch operation, this contact resistance should be minimized. Thermal contact resistance has been studied for gold coatings on ceramic substrates, for example Al_2O_3 [17]. Here, thermal contact resistance was studied and correlated with adhesion and the nature of the interface domain. Lower thermal contact resistances and stronger adhesion were reportedly obtained by ion etching the substrate before deposition. The surface roughness of the substrate was reported to be 78nm. Annealing of the gold film was performed after evaporation deposition. The contact resistance measurement was performed using a pulsed laser procedure and measuring the electrical resistance of the metal layer as the metal cooled. Over a range of metal thicknesses from 100 to 400nm, a minimum contact resistance was found for a film thickness around 200nm, and the resistance measured was less than 1e-7 m^2K/W.

Equally interesting to this research is the thermal contact resistance behavior of smooth, polished surfaces in close contact. Theories have been developed to predict this behavior but agreement with experiments has been inconsistent. Some of these theories have been summarized by Wolff [18]. One theory modeled the contact as asperities touching at the interface. Conduction depended on contact pressure, thermal conductivity, hardness, surface finish, along with size and shape of the contact asperities. Lumped parameter methods became highly useful in developing this theory. Actual measurement work then proceeded by measuring the conductivity across the interface of

differing materials and several interstitial fluids. The variety of surface finishes adds a degree of complexity to modeling this phenomenon. For example, bead blasted surfaces tend to have homogeneous distributions of asperities, but ground and sanded surfaces have directionally dependent roughness that make prediction more difficult.

It has been observed that for very smooth surfaces and very hard materials, applied pressure has little effect on the contact resistance [18]. Pressure only tends to affect contact resistance for materials with rougher surfaces that can easily deform at either microscopic or macroscopic levels. Conclusions of experimentation [18] have lead to a belief that the ability of the interface material to conform to the opposing surface material is more important than the conductivity of the materials themselves.

Literature reports that thermal aging can affect the contact resistance of cobalt and nickel hardened gold platings (called hard golds) on copper [19]. This may provide another avenue to explore for reducing contact resistance. Electrodeposited gold containing nickel and cobalt were deposited and aged at a variety of temperatures. At temperatures between 150° and 200°C, the aging effect actually caused the contact resistance of the hard golds to increase over the contact resistance of pure gold. The hardeners themselves increased the contact resistance of pure gold as well. Contact resistance was measured by a probing technique specified in ASTM B-667. Longer aging duration also caused increases in thermal contact resistance of the hard golds, where pure gold remained constant.

Measuring contact resistance is a difficult process. However, characterizing the contact resistance in a thermal switch is very important. A laser-based, non-contact and non-destructive transient thermo reflectance (TTR) method has been used to measure

thermal conductivity of a variety of silicon types and their oxides, as well as thermal contact resistance between a blanket gold layer and the silicon oxide layer [20]. Specifically, the silicon-28 isotope in a purified form was tested and compared with natural silicon, which has a mixture of all silicon isotopes. The results showed that silicon-28 has an increased thermal conductivity, as well as a decreased thermal contact resistance with a deposited gold layer, over natural silicon.

1.2.4 Thermal Interface Materials

A variety of new thermal interface materials (TIMs) are being studied that hold the promise of increasing performance of thermal switches. TIMs are used to reduce contact resistance in order to optimize thermal switch performance.

One TIM that is currently being studied is carbon nanotubes (CNT). CNT's have high thermal conductivities, high aspect ratios, as well as good mechanical strength that provide attractive characteristics for improved thermal control applications. They can be grown from a catalyst thin film and usually form a surface structure like a forest or grassy turf [21]. CNT's could provide a compliant, elastic interface for contact of a thermal switch, which has potential to reduce wear and fatigue of the contacting surfaces. CNT's have yet to be integrated into a thermal switch, but the mechanical and thermal properties of CNT's could be advantageous. Densely grown CNT turfs could provide a surface that would conform well to asperities of solid contacting surfaces and reduce contact resistance.

Another TIM, known as curable polymer gels, is also being studied [22] to replace more traditional thermal greases [23] in electronics. These gels have different mechanical properties due to differences in the rheology of polymers. Their behavior

transitions from a grease to a gel when cured. These TIMs are intended to be used at the interface between microprocessors and the heat sinks used to dissipate the thermal power generated during operation.

Polymer-based-gel TIMs have high bulk thermal conductivities and low thermal interface resistances. When applied to the heat sink assembly, these gels are in a grease form. They have low surface energies and conform well to surface irregularities, which minimizes thermal contact resistance. Once they cure, the gels crosslink into a filled polymer, allowing cohesive strength that avoids the leaking issues exhibited by greases during temperature cycling. The thermal contact resistances for these gels are typically measured between 1 and 5e-5 m^2K/W at pressures up to 700 kPa [22]. The characteristics of these materials may not lend similar benefits to thermal switches like CNT's, but perhaps they could be useful at the interface between a thermal switch and the connected bulk thermal reservoir. Low contact resistance between the heat source and the thermal switch could be beneficial in cooling applications as in spacecraft thermal control discussed earlier.

The TIM used in the thermal switch of this research is mercury. Mercury droplets form a compressible contact for the thermal switch because they are in a liquid state at room temperature. This compliant contact reduces the threat of physical wear on the thermal switch and contacting surface. Likewise, the liquid state of mercury allows the droplets to easily deform when in contact. Contact area is allowed to increase as separation distance decreases, which both lower thermal resistance and increase thermal switch performance. Additionally, the liquid mercury can more easily conform to the irregularities of the contacting surface, which decreases contact resistance.

The thermal switch discussed in this thesis utilizes arrays of mercury micro droplets that are deposited on a silicon substrate. The fabrication of the mercury micro droplet arrays has been previously developed [24,25].

1.2.5 Characterization of MEMS Mercury Micro Droplet Switch

The development and characterization of the mercury droplet array thermal switch was inspired by the application of mercury micro droplets in a MEMS electrical switch [26, 27]. The deposition process for forming microscale mercury droplets was developed [26]. A model of the mercury micro droplet's mechanical behavior was developed and reported by J. Simon [28].

$$a = \frac{d\cot\phi}{4} - \frac{d\pi}{18\sin^2\phi} \pm \sqrt{\frac{V}{d\pi} + \frac{d^2\pi^2}{324\sin^4\phi} + \frac{d^2\pi\cos\phi}{36\sin^3\phi} - \frac{d^2\cot^2\phi}{48} - \frac{d^2}{6\sin^2\phi}} \qquad 1.1$$

This model describes the relationship between contact radius **a,** droplet height **d**, contact angle **θ**, and volume **V** of a single mercury droplet. The force required to deform a single mercury droplet can be found from the capillary pressure difference across a liquid surface, which is given by N. Adam [29]:

$$\Delta P = \gamma\left(\frac{1}{R_1} + \frac{1}{R_2}\right) \qquad 1.2$$

The capillary pressure difference **ΔP** is a function of the surface tension **γ** and the two principle radii of curvature $\mathbf{R_1}$ and $\mathbf{R_2}$, which define the shape of a sphere.

1.3 Research Objectives

This research investigates the mechanical and thermal behavior of a thermal switch based on arrays of liquid metal micro droplets deposited on silicon substrates. The droplet arrays provide a compliant contact between a heat source and a contacting surface.

Mechanical behavior involves both static and dynamic characterization of the droplet arrays. The static relationship between the force applied to deform the droplets, the contact area, and the deflection is investigated. Statistical characterization of the droplet arrays is also performed. Mechanical models are then developed to validate the experimental characterization. Dynamic characterization of the micro droplet arrays is also performed. This consists of cyclic actuation of the thermal switch to characterize long term switching behavior and longevity.

Thermal behavior is studied by developing a thermal model to predict the thermal resistance of the switch with respect to the force applied during contact. The thermal model is developed from the mechanical and statistical characterization of the droplet arrays. Thermal resistance is calculated for the entire thermal switch at different applied static contact forces. This model is compared with experimental measurements of thermal resistance obtained by T. Wiser through the use of a guard heated calorimeter [30].

CHAPTER 2

FABRICATION

2.1 Overview

MEMS technology is built on the backbone of the IC industry and the silicon-based fabrication techniques that have been developed and used for the last 30+ years. What has helped make microprocessor technology so affordable has been the ability to batch manufacture these microprocessor chips. MEMS technology boasts the same capability to reduce costs and increase production of devices. Processing of a single wafer can produce many individual devices that can be tested and used individually.

The liquid metal micro droplet arrays used in the thermal switch are fabricated using a few techniques that have been the basis of IC fabrication for decades. While thin film metal deposition can occur in a variety of different ways, magnetron sputtering is one traditional method that is used in this research. Photolithography is the process where a pattern is transferred to the substrate from a mask. Selective etching of the metal thin film during photolithography produces various shaped structures on the substrate. Finally, the liquid metal is deposited on the substrate via evaporation and selective condensation. The liquid metal used in this research is mercury, and the condensation targets are gold, to which mercury has a very strong chemical attraction. These fabrication processes will be further discussed in detail below.

2.2 Thin Film Deposition

Mercury droplet deposition occurs by preferential condensation of mercury vapor onto gold target pads that are fabricated on a silicon wafer substrate. The silicon wafer has been previously covered with a thermally grown silicon oxide layer. The gold layer

and a titanium-tungsten adhesion layer are deposited onto a silicon substrate by DC magnetron sputtering. The sputtering system consists of a sealed, evacuated chamber where the silicon wafer is positioned above the metal source targets. Once the chamber is evacuated to a prescribed pressure, argon gas is brought into the chamber. A voltage field is created which attracts argon ions. The argon ions then accelerate into the metal source target and detach metal atoms that spray up towards the silicon substrate. Longer deposition times allow for a thicker metal layer to be deposited on the silicon substrate. The TiW layer is deposited first for 51 seconds then the gold is deposited for 21 minutes to obtain thicknesses of 5nm and 300nm, respectively.

2.3 Ultra-Violet Photolithography

Once the thin film layer of gold is deposited onto the silicon wafer, ultraviolet photolithography is used to define the deposition target pads. A polymer photoresist, AZ5214, is deposited on top of the gold by a spin coating technique at 3000 RPM for 30 seconds and then hardened by baking on a hotplate at 110°C for 1 minute. A transparency mask, shown in **Figure 2.1**, is then used to cover the wafer when exposed to ultraviolet light for 12 seconds. **Figure 2.2** shows a magnified image of the mask for a single square grid array on a die with dimensions of 10mm by 18mm. The mask is a printed image on a transparent polymer sheet that allows light to pass through and expose selected areas of the wafer while masking light exposure from other areas of the wafer. When light passes through the transparency mask and exposes the photoresist layer, cross linking within the photoresist polymer breaks apart.

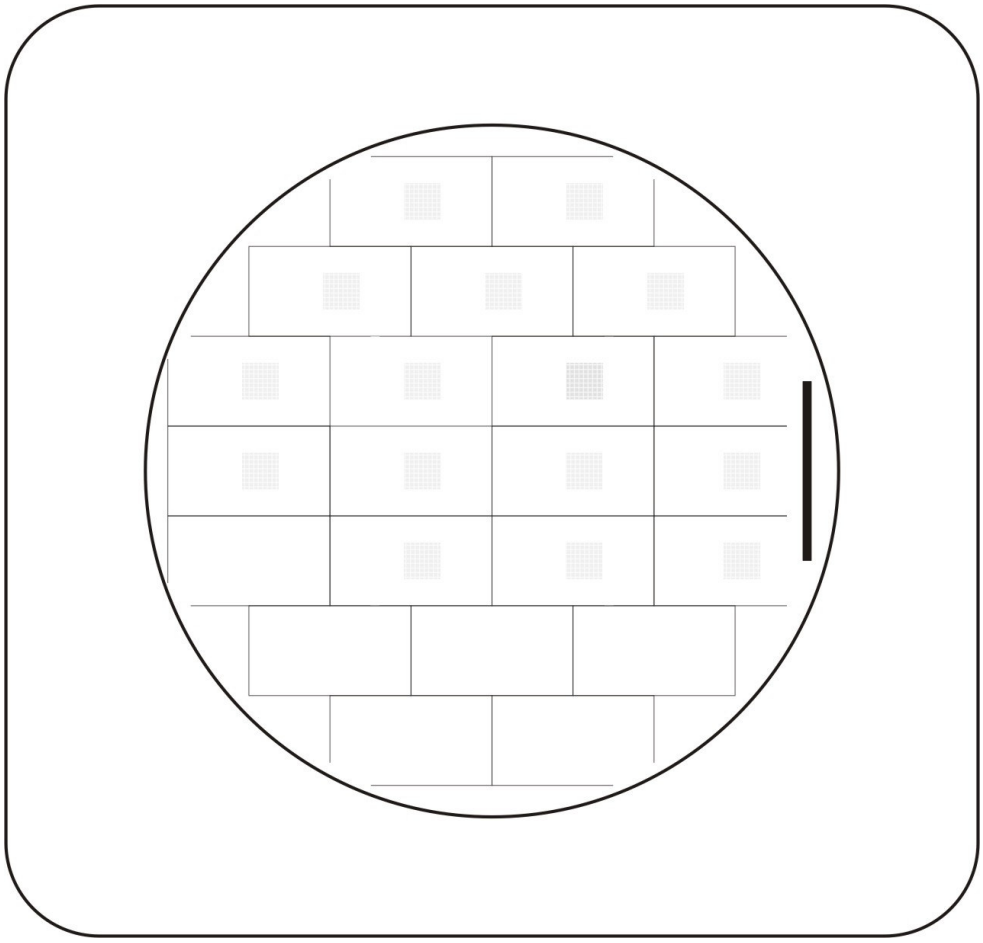

Figure 2.1: 1600 Droplet Array Gold Mask

The exposed areas of the photoresist are etched away when the wafer is immersed in a solution of one part photoresist developer, AZ400K, to four parts deionized (DI) water. The unexposed areas are unaffected by the developer solution. The mask feature size is limited by printer resolution, so during development, the photoresist is overetched. This reduces the size of the deposition pads to a diameter between 5 and 10 microns. It has been determined that this is an optimal gold target size to obtain consistent droplet growth during mercury deposition. The developed pad diameter is carefully controlled by monitoring the development process with a microscope. If the photoresist pads are too large, the wafer is immersed again in the developer solution for short periods of time

until the pads are the proper size. The pad size is constantly monitored using a microscope.

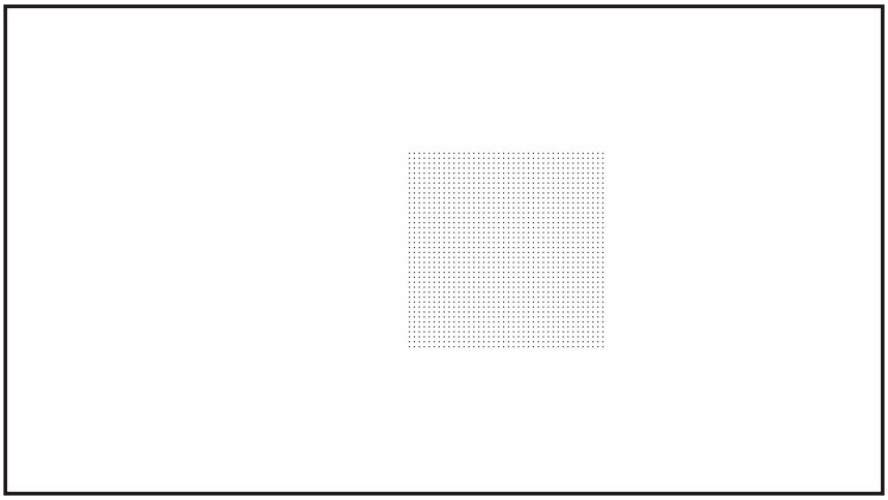

Figure 2.2: 1600 Droplet Array Die Mask

The result is a wafer with a blanket layer of gold and a patterned layer of photoresist. Some portions of the gold are covered by photoresist while other portions of the gold are exposed to the environment. The wafer is then immersed into a gold etch solution to etch away the areas of exposed gold. The gold areas covered by photoresist are unaffected and thus remain after etching has completed. The wafer is rinsed in DI water and is then immersed into hydrogen peroxide. This process step etches away the titanium-tungsten adhesion layer from the areas where gold was etched away. The silicon dioxide layer of the wafer is then fully exposed. The remaining photoresist is easily washed away using a standard five step acetone/IPA/DI/acetone/IPA cleaning process.

The remaining structure on the wafer is a pattern of the gold pad arrays on top of silicon dioxide, in the same pattern as the mask shown above. Another photolithography step is performed to protect the exposed oxide layer from mercury deposition. The gold etching does not always remove all remnants of gold from the exposed areas. This can

potentially attract mercury vapor to deposit additional droplets on the substrate, which are referred to as satellite droplets.

Satellite droplets can be potentially hazardous to the operation of the droplet arrays when the thermal switch is actuated against the P3 micro heat engine. If a satellite droplet sits near another droplet on a gold pad, the two droplets can touch and quickly combine into a larger droplet when deformed with enough force during operation. If these droplets continue to grow by combining with other droplets, eventually the droplet array can deteriorate into a large mercury puddle that will wash over the entire array surface, engulfing all other droplets.

Due to the limited actuation distance of the thermal switch, these large puddles will never break contact with the P3 engine. The result is a thermal switch that never switches. In essence, there would never be an "off" state, because the mercury would always keep the engine and the switch surface in constant contact. This would severely hinder the performance of the P3 engine, which needs cyclic heat addition in order to run. Continuous heat addition will cause the mean temperature of the P3 engine to rise. The engine will not be able to reject heat fast enough to keep up with the heat addition. The engine will stop oscillating and remain in a perpetually expanded shape.

For this reason, a method was found to prevent satellite droplet formation during mercury deposition. Mercury has shown little tendency to condense on hardened photoresist. Photoresist is spun over the top of the wafer again. The photoresist acts as a protection layer over the oxide and minimizes satellite deposition. Using an inverted image of the mask used in the gold patterning process described before, holes in the photoresist are patterned to expose the previously formed gold pads. **Figure 2.3** shows

the array section of the inverted mask. Overetching in the photoresist developer widens the holes in the photoresist to a diameter slightly larger than the diameter of the gold pads. This is monitored with a microscope like the previous development process until the gold pads are fully exposed through the photoresist holes. Aligning this mask with the existing gold dots is important for this process. The mask aligner machine has a high resolution positioning system and microscope for this task.

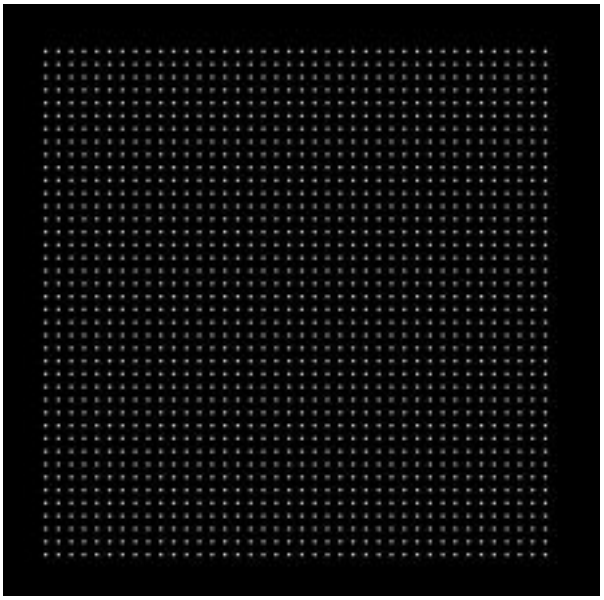

Figure 2.3: Photoresist Protection Layer Die Mask

Once this final patterning step is performed, the wafer is cut into die. Each die has a single gold pad array centered in the middle. The die cannot be cleaned using the standard five step acetone/IPA cleaning process, because the photoresist protection layer would be washed away. So cleaning the die prior to deposition consists of rinsing the die under DI water for 2 minutes. The die is then immediately exposed to mercury vapor to reduce contaminants on the surface of the die. These can provide locations for satellite droplet formation which must be minimized.

2.4 Droplet Deposition

A cleaned and patterned die is exposed to mercury vapor to deposit the micro droplet array. A sealed chamber with a pressure release cold trap attached is heated in an oil bath inside a fume hood. A small puddle of mercury sits at the bottom of the sealed chamber. A Teflon plate covers the top of the chamber and is sealed with o-rings. The die is placed over a hole in the Teflon plate on top of an o-ring to provide a seal. The die is then clamped down against the Teflon plate with a third o-ring, a metal bar, and two bolts. There is a shutter on the bottom side of the Teflon plate which is controlled from the outside by a magnetic clip. The shutter can slide lengthwise along the bar clamp, and it is held in place beneath by a grooved track. A diagram of the mercury deposition chamber is shown in **Figure 2.4**.

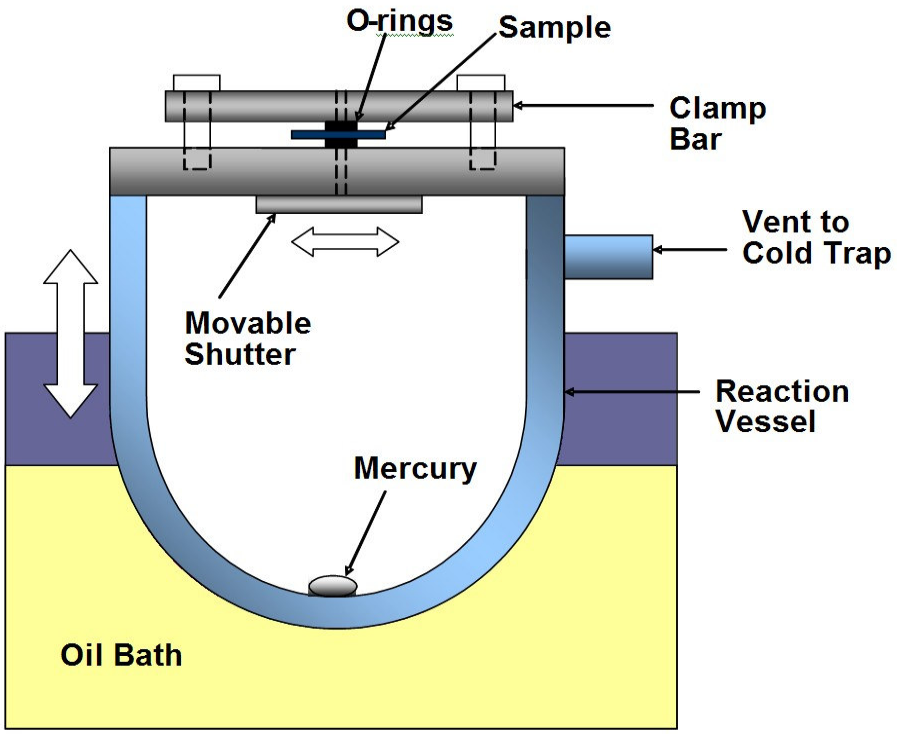

Figure 2.4: Mercury Deposition Chamber

The deposition process is performed first by carefully placing the die over the o-ring and hole of the Teflon plate. The gold pad array must be centered inside the o-ring to ensure optimal droplet deposition and consistency in size. If the array is offset in any direction, the gold pads closest to the o-ring will potentially have less mercury deposited. The die is clamped down and the shutter is tested to ensure the magnetic contact with the clip is secure. The shutter is moved over the hole to deflect any mercury deposition from occurring during heating.

The oil bath is quickly heated to 176°C. Once the oil bath has reached a steady state temperature, then the shutter is opened for a specified amount of time. Different array sizes require different amounts of time for deposition. With more gold pads present, more mercury must be deposited, so more time is required. For the standard 1600 droplet arrays (40x40 square grids) used in this research, a deposition time of 60 minutes consistently produces uniform droplet arrays.

The deposition occurs by the evaporation of the heated mercury as it tries to achieve equilibrium. This is driven by differences in the equilibrium partial pressures of the mercury vapor and air atmosphere inside the chamber. When the mercury evaporates, it does so in all directions. However, the hole in the Teflon plate is significantly smaller than the surface area of the mercury puddle beneath in the chamber. The distance between the mercury source and the hole is also very large with respect to the diameter of the hole. This means the mercury vapor that is entering the hole and depositing on the die on the other side is diffusing vertically and very little in any other direction. For this reason, the gold pad array should be centered over the hole, both which are of similar

dimension. If there is an offset, the gold pads not in direct line of sight of the mercury puddle beneath will have very little mercury deposited.

CHAPTER 3

THERMAL MODEL

3.1 Overview

The major goal of this research is to develop a theoretical model to predict the thermal resistance of a thermal switch as a function of applied load. This model could then be used to design and optimize an effective thermal switch. An optimized thermal switch would transfer the maximum amount of heat into and out of the P3 micro heat engine at the appropriate times in order to maximize engine performance and efficiency.

When designing an effective thermal switch, it is necessary to maximize the thermal resistance of the switch in the "off" position. This "off" position occurs when there is a gap between the thermal switch and the contacting surface. Likewise, the thermal resistance must be minimized in the "on" position, when the switch and the contacting surface make contact. Achieving the largest thermal resistance ratio of the "off" to "on" states will maximize the engine performance by optimally controlling the heat transfer into the engine.

3.2 Method

The theoretical model described here incorporates three main factors that are used to predict thermal resistance as a function of applied force on a mercury micro droplet array thermal switch. First, analytical solutions of the mechanical behavior of a single droplet are found. The mechanical behavior involves relating the geometric shape of a deformed droplet to the force required to cause the deformation. Second, a statistical analysis of the droplet size distribution in the square grid droplet array accounting for droplet size, position, and population is described. Third, the mechanical behavior and

the statistics of the droplet arrays are used to calculate thermal resistance for an entire droplet array.

The mechanical behavior of a single droplet can be described by two equations, which will be presented and discussed in more depth below. The first equation deals solely with geometry and describes the relationship between droplet contact diameter and gap length. Gap length is equivalent to the deformed droplet height or the length of the heat path. The second equation relates the internal capillary pressure to the two radii of curvature of a deformed droplet. Combining these two equations for capillary pressure and contact area, the force applied to deform the droplet to a given deflected height can be found.

Droplet statistics are then employed to apply the single droplet results to an array of droplets with a distribution of diameters. Statistically characterizing the variation in droplet diameters enables accurate predictions of mechanical behavior for an entire droplet array.

The thermal behavior of a droplet array is then characterized using the concept of a thermal network. Each droplet and the surrounding gas are represented by a parallel thermal resistance.

3.2.1 Mechanical Behavior

Thermal behavior of the thermal switch is closely coupled to the mechanical behavior of the droplets. Thus, it is imperative to understand the mechanical behavior in order to predict the thermal behavior of the thermal switch. The thermal resistance of a droplet depends on the heat path length or droplet height, the cross sectional area of the heat path or the droplet contact area. Therefore, to calculate droplet thermal resistance at

any applied load requires an analysis of the mechanical behavior of a deformed droplet. For this reason, the force applied to the droplet and its corresponding effect on the deflection and contact area of the droplet is characterized.

3.2.1.1 Geometry

The geometry of a deformed mercury micro droplet is considered first. The droplet is assumed to be between two parallel rigid plates that are brought together. As the two plates come into contact with the droplet, the droplet is deformed. First, the height of the droplets decreases as it is squeezed between the plates. Second, the contact area between the droplet and the plates increases. **Figure 3.1** represents the cross sectional geometry of the deformed droplet as it is squished towards the y-axis.

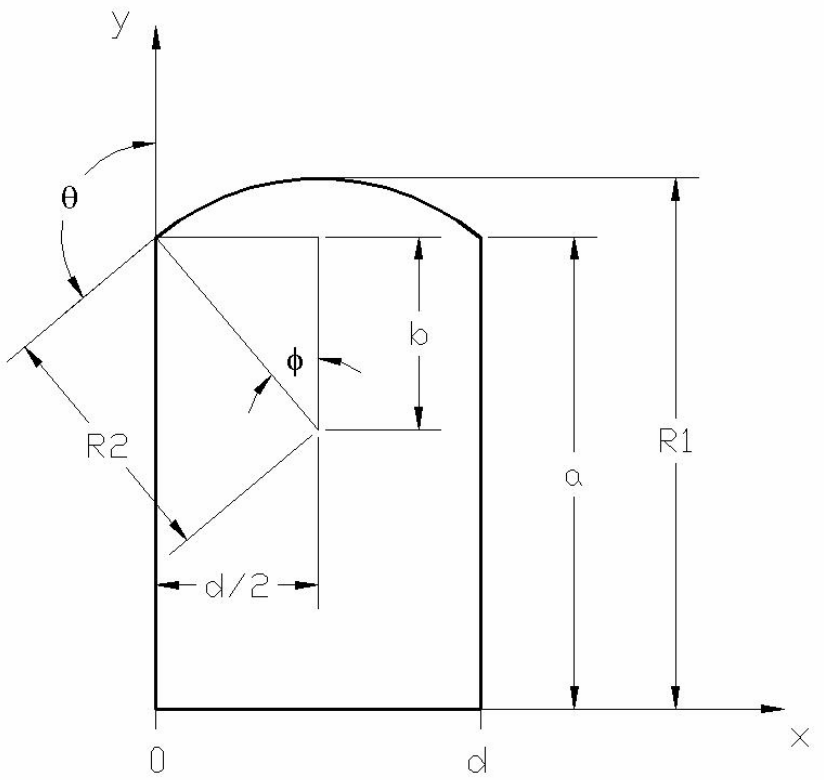

Figure 3.1: Two Dimensional, Axisymmetric Representation of Deformed Droplet

Rotating the area below the circular arc (between x=0 and x=d) around the x-axis produces the volume of a droplet deformed under an applied load between two parallel plates. The volume of this rotated region is given by:

$$V = \int_0^d \pi[f(x)]^2 dx \qquad 3.1$$

The profile of the deformed droplet f(x) is described by:

$$f(x) = \sqrt{\left(\frac{d}{2\sin\phi}\right)^2 - \left(x - \frac{d}{s}\right)^2} + \left(a - \frac{d}{2\tan\phi}\right) \qquad 3.2$$

where the function **f(x)** is the equation for a circle, centered at **(d/2, a-b)** as shown in the appendix. Inserting **Equation 3.2** into the integral in **Equation 3.1** and evaluating gives:

$$\frac{V}{\pi} = a^2 d - \frac{ad^2}{\tan\phi} + \frac{ad^2}{2\tan\phi} + \frac{ad^2\pi}{9\sin^2\phi} + \left(\frac{d^3}{4\sin^2\phi} - \frac{d^3}{12} - \frac{d^3\pi\cos\phi}{18\sin^3\phi}\right) \qquad 3.3$$

as shown in the appendix. Rearranging this solution in terms of **a** as a function of **d**, **ϕ**, and **V**, yields [28]:

$$a = \frac{d\cot\phi}{4} - \frac{d\pi}{18\sin^2\phi} \pm \sqrt{\frac{V}{d\pi} + \frac{d^2\pi^2}{324\sin^4\phi} + \frac{d^2\pi\cos\phi}{36\sin^3\phi} - \frac{d^2\cot^2\phi}{48} - \frac{d^2}{6\sin^2\phi}} \qquad 3.4$$

as shown in the appendix. **Equation 3.4** gives a relation for **a**, the contact radius, in terms of **d**, the deflected droplet height, which is also equal to the gap length between the two parallel plates. In the derivation, constant volume **V** of the droplet and constant contact angle, **θ**, were assumed. Constant volume **V** follows from conservation of mass. Constant contact angle **θ** follows from the fact that the contact angle is a property of the interface between a solid, liquid, and gas. In this case, the interface is between air, mercury, and SiO_2. The angle **ϕ** can be found from **θ** using:

$$\phi = 90 - [180 - \theta] \qquad 3.5$$

as shown in the appendix.

3.2.1.2 Force

The force required to deform a droplet depends on both the internal pressure and the contact area of the droplet. The internal pressure of the droplet is due to capillary forces. The capillary pressure in the droplet depends on the surface tension **γ** and the two radii of curvature of the spherical droplet, $\mathbf{R_1}$ and $\mathbf{R_2}$ [29]:

$$\Delta P = \gamma(\frac{1}{R_1} + \frac{1}{R_2}) \qquad 3.6$$

The pressure difference **ΔP** is the difference between the pressures acting on the inside and outside of the droplet surface, or the difference between the internal capillary fluid pressure of the droplet and the external atmospheric pressure. The surface tension **γ** for mercury is 0.48 N/m [31]. The two radii of curvature $\mathbf{R_1}$ and $\mathbf{R_2}$, are shown in **Figure 3.2**.

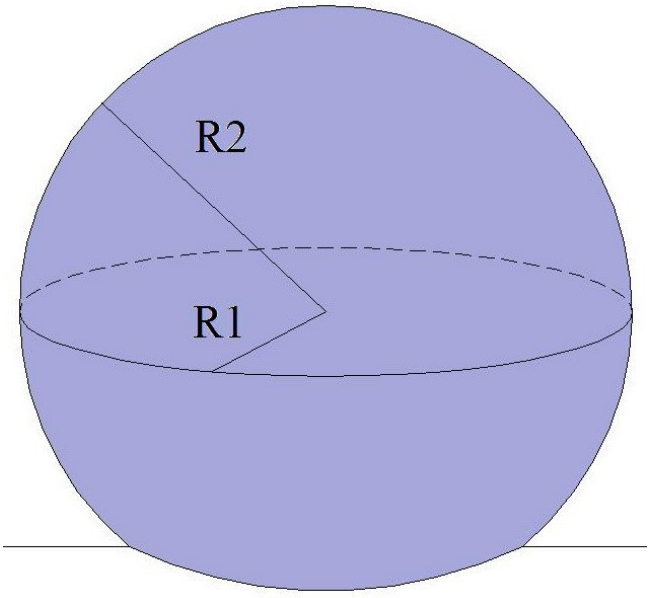

Figure 3.2: Principle Radii of Curvature for a Sphere

The two radii of curvature can be mathematically calculated using trigonometry as shown in the appendix. Solving **Equation 3.6** for the static pressure inside the droplet gives:

$$P_{drop} = \gamma(\frac{1}{R_1} + \frac{1}{R_2}) + P_{atm} \qquad 3.7$$

The force applied to the droplet is calculated by multiplying the droplet pressure by the contact area:

$$F = P_{drop}(\pi a^2) \qquad 3.8$$

3.2.1.3 Deflection

Deflection δ is calculated by subtracting the deformed droplet height **d** from the original droplet height **h**, which is a function the original droplet diameter $\mathbf{D_0}$:

$$h = \frac{D_0}{2}(1 + \sin\phi) \qquad 3.9$$

A graphical representation of **Equation 3.9** is shown in **Figure 3.3**. Height is the sum of the two terms shown in the figure.

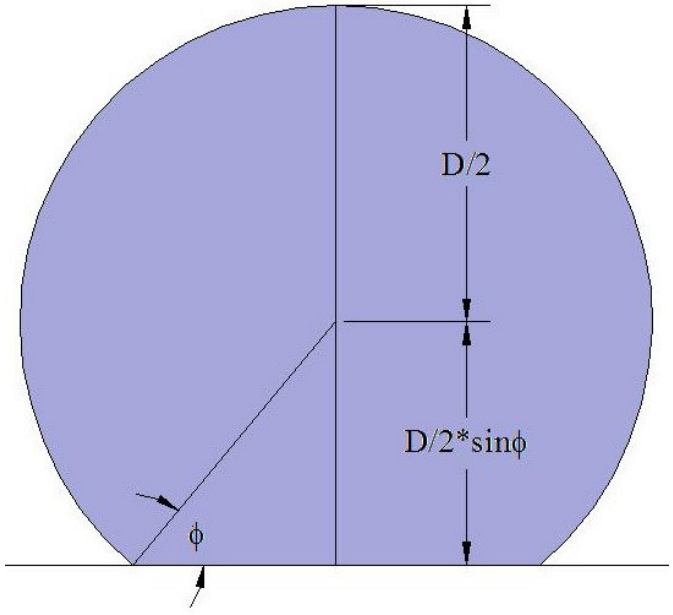

Figure 3.3: Diagram of Droplet Height Calculation

3.2.2 Droplet Array Statistics

The thermal switches used in this research were fabricated with arrays of approximately 1600 micro droplets. Within each array, the micro droplet diameters varied around a mean nominal droplet size. The distribution of droplet diameters was characterized for each micro droplet array by measuring the diameters of a sample population of droplets. Droplet diameters were measured by capturing digital pictures of representative portions of the droplet array using an optical microscope and digital camera. Droplet diameters, as well as the number of droplets found on a given Au target or deposition site were determined. The mean droplet diameter was calculated for the sample using [32]:

$$\bar{y} = \frac{\sum_i y_i}{n} \tag{3.10}$$

The standard deviation of droplet diameters was calculated using [32]:

$$s = \sqrt{\frac{1}{n-1}\sum_i \left(y_i - \bar{y}\right)^2} \tag{3.11}$$

where n was the sample population.

The sample droplet diameters were plotted in histograms with bin sizes of 2 microns. Histograms were normalized by dividing bin populations by the total number of droplets sampled, to give percentages. The number of excess droplets in the sample was also found. Since the expected total population of the entire droplet array was 1600, the ratio of actual sample size over expected sample size was multiplied by 1600 to estimate the actual array population. The same procedure was used to estimate the global population for each bin.

3.2.3 Thermal Behavior

The thermal resistance across a micro droplet array is found by constructing a thermal resistance network that accounts for 1) droplets that are squeezed between two plates and touch both plates, 2) droplets touching one plate but not the other, and 3) the gas filling the gap between the two plates. A simplified example showing two droplets and the associated thermal resistance network is given in **Figure 3.4**. Each of the above three cases is considered separately. Then, a method to account for the statistical distribution in droplet diameters is discussed.

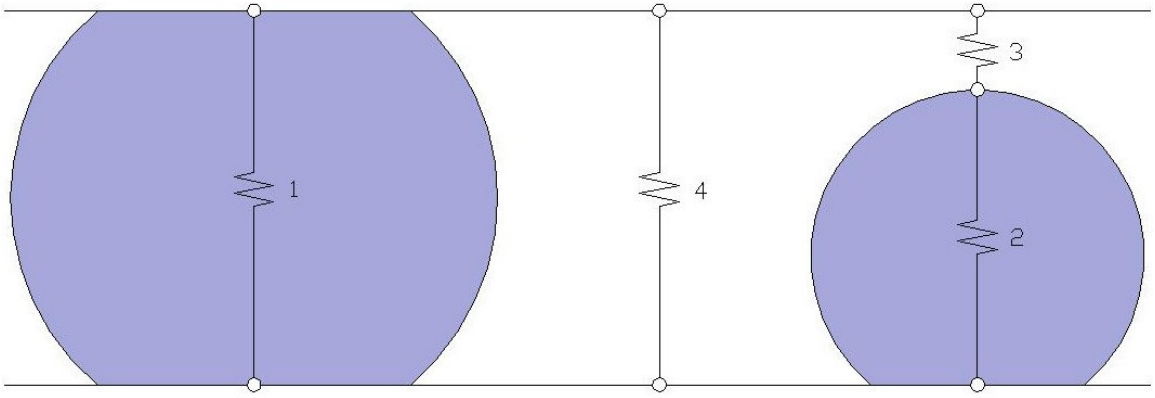

Figure 3.4: Thermal Resistance Network

The thermal resistance of a droplet depends on the conduction path length through the droplet, the thermal conductivity, and cross sectional area of the droplet, which is given by:

$$R_{th} = \frac{L}{kA} \qquad 3.12$$

The thermal resistance of a droplet was determined by approximating the droplet's deformed shape as a cylinder. However, since a deformed droplet is not a straight cylinder but rather has a curved "barrel" shape (due to the constant contact angle property of the material interface), two thermal resistance calculations for the droplet is

made for each plate position. First, the thermal resistance of the smaller cylinder based on the contact radius **a** of the droplet is calculated. Second, the thermal resistance based on the largest radius of the "barrel" shape, $\mathbf{R_2}$, is found. These two values provide an inner and outer bound to the problem. The two values are then averaged to obtain an approximation of the real droplet array thermal resistance.

Because there is a distribution of droplet heights, some droplets are in contact with both plates while other droplets are not in contact. Thus, there is a small gap of gas between some droplets and the contacting plate surface. This air gap thermal resistance, in series with the droplet beneath it, is included. The thermal model assumes that the cross sectional area of this air gap is the same as the area of the droplet cylinder, depending on the case for which droplet cylinder is used.

As mentioned previously, it is equally important to include the thermal resistance of the gas gap in the model calculation. While the droplets account for a majority of the change in thermal resistance with increasing force, the effects of the gas are included to obtain additional accuracy in the prediction. Two factors are considered in relation to the gas effects. First, the droplets do not cover the entire surface area of the thermal switch. Experimentally, the surface area of the 1600 droplets ranges from less than one percent initially up to five percent when deflected by 1N of force. So a large proportion of the surface area is covered by air, which has a different thermal resistance than mercury.

When considering an array of droplets with varying size, the path length and cross sectional area are calculated with respect to force for each statistical bin of similarly sized droplets. The path length of the bin is the same as any single droplet in the bin at a given deflection. However, the cross sectional area of the bin is obtained by multiplying the

contact area of a single droplet by the population of the entire bin. The thermal resistance is then calculated for each bin using the path length and the total cross sectional area of the bin by **Equation 3.12**. The value for the thermal conductivity **k** of mercury is 8.54 W/mK [33]. These calculations are repeated for every bin over a range of different deflections.

Because the droplet size of each bin is different from one bin to the next, the statistical variation of droplet size among all bins is important to include in the model. Here, the variation in droplet height is considered. At the start of the model, the thermal resistance is calculated with a gap of 2 microns separating the plate and the tallest bin of droplets. Next, the thermal resistance is calculated when the plate moves 2 microns closer. Here, the plate makes contact with the tallest bin of droplets but does not deform them. Again, the plate is moved closer. The first bin of droplets is deformed until the second bin of droplets is touched, which is shorter than the first. The thermal resistance is calculated again. Subsequent calculations of thermal resistance are performed in similar fashion through contact of each bin of droplets. As more droplets come into contact with the plate, the thermal resistance decreases due to a greater number of paths for the heat to transfer through. Likewise, the taller bins of droplets continue to deform, decreasing path length and increasing contact area, which also causes the thermal resistance to decrease.

Once all the requisite thermal resistances are accounted for, the single effective thermal resistance for the switch is found using the techniques employed with the electrical resistance analogy. Resistances that are in series are summed together directly (droplets not in contact with the second plate, along with the gas gap between the droplet

and the plate) to form a single combined resistance. An equivalent thermal resistance for all parallel thermal resistances, $\mathbf{R_n}$, (droplets in contact, droplets not in contact, and the surrounding gas gap) is calculated by:

$$R_{eq} = \frac{1}{\left(\frac{1}{R_1} + \frac{1}{R_2} + \ldots + \frac{1}{R_n}\right)} \qquad 3.13$$

For each plate position, thermal resistance is plotted with respect to force applied to deform the droplet array. Thus, as the two parallel plates move closer together, a range of plate positions was used to calculate thermal resistance and force. Three separate curves are plotted, one based on each of the two cylindrical radii, and the third based on the average of the two cylindrical approximations.

CHAPTER 4

EXPERIMENTAL APPARATUS

4.1 Overview

A goal of this research was to characterize the mechanical behavior of mercury micro droplet arrays. Square grid arrays of 1600 droplets were characterized under static and dynamic loads. Force, deflection, and contact diameter was measured and then used to validate the model for the parameters described in the previous chapter. The arrays were composed of nominal 30μm diameter droplets. A second set of measurements were made on large droplets with diameters on the order of 200μm.

Two sets of experiments were conducted for this research: 1) static characterization and 2) dynamic characterization of the mercury droplet arrays. The goal of both of these experiments was the same, to visualize the droplets and characterize their behavior when deformed. The apparatus used for static characterization of the micro droplets is discussed first. The apparatus used for the dynamic characterization of the micro droplets is discussed next.

4.2 Static Deformation

Mechanical characterization of the droplet arrays under static deformation consisted of applying a known force to deform the droplets, and then measuring the resulting deflection (or decrease in height), and the increase in contact area. A diagram of the static deformation apparatus used to make measurements is shown in **Figure 4.1**. The droplet arrays were mounted on top of an aluminum bracket, which was attached to the top of a load cell and a z-axis optical positioning stage. A glass slide was mounted above the z-axis stage on the bottom of an aluminum plate with a slotted hole machined

into the center for optical access. The slot was made as small as possible so that deflection of the glass would be minimized.

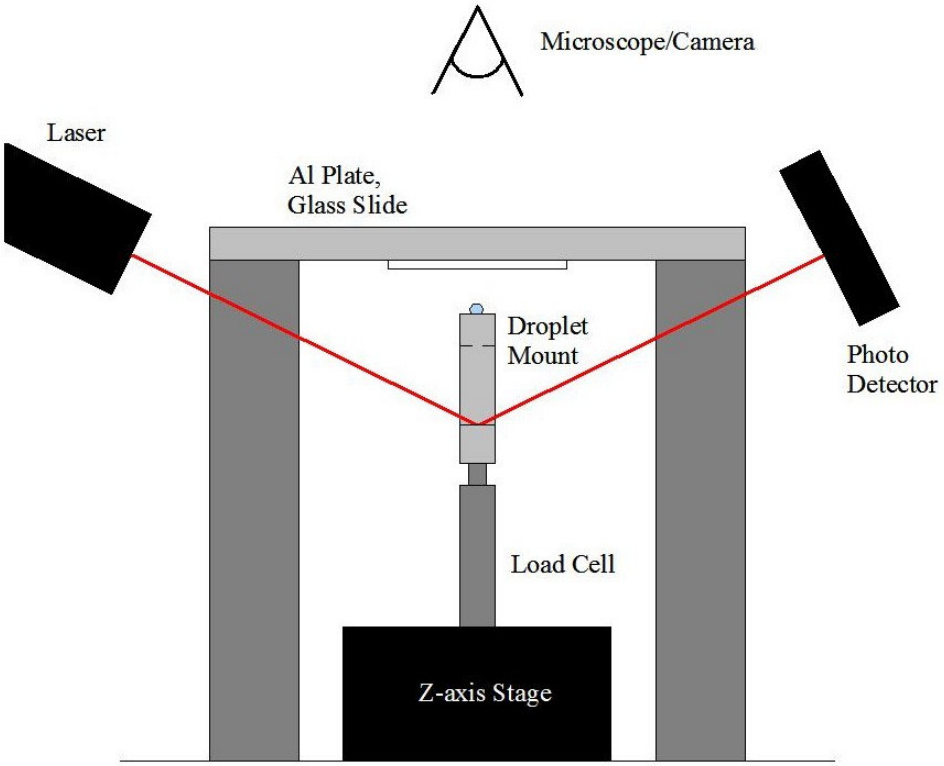

Figure 4.1: Static Deformation Apparatus

The plate was bolted into four, 1 inch diameter steel optical posts that were attached to an optical air table. With the droplets and z-axis stage positioned beneath the glass slide and aluminum plate slot, the z-axis stage micrometer was used to raise and lower the droplets. The droplets were brought into contact with a glass slide, which provided a flat, rigid, and transparent surface for visualization. A microscope and digital camera centered directly above the slot was used to image the droplets. A load cell, mounted in series with the droplet array, was used to measure the applied force. A laser and photo detector system was used to measure the displacement of the droplet arrays.

4.2.1 Compliance

In order to obtain accurate measurements of the force-deflection relationship of the droplets, it was important to minimize the compliance of the test stand. A simple beam deflection analysis was performed on the top plate to determine a plate thickness that would deflect less than 2μm under the applied loads in the droplet experiments. Maximum deflection $\mathbf{v_{max}}$ of a simply supported beam with a length of **L**, under a load of **P** located at the center of the beam, with elastic modulus **E** and moment of inertia **I**, is given by[34]:

$$v_{\max} = \frac{-PL}{48EI} \tag{4.1}$$

The maximum deflection of the glass slide was found by assuming that the load applied to the glass slide was 0.125 inches away from one end of the slot, based on the position of the die under the slot. The maximum deflection would then be found by [34]:

$$v_{\max} = \frac{-Pba\left(L^2 - b^2 - a^2\right)}{6EIL} \tag{4.2}$$

where **b** and **a** are the distances from the load to either end of the beam. The load applied to both the glass slide and the aluminum plate was taken to be 0.1 N, the maximum applied load for the static deformation experiments. The length of the aluminum plate was 5 inches, the largest dimension diagonally. The length of the glass slide was assumed to be 0.5 inches, the length of the slot in the plate. The elastic moduli of the aluminum and the glass were both taken to be 70 GPa. The moments of inertia for aluminum and glass were calculated by [34]:

$$I = \frac{1}{2}Lt^3 \tag{4.3}$$

and equalled 9.14×10^{-9} m^4 and 8.46×10^{-12} m^4, respectively, where **L** is the base length, and **t** is the height (or thickness of the plate). The thicknesses of the aluminum plate and glass slide were 9.525 mm and 2mm, respectively. The respective maximum deflections for the aluminum plate and the glass slide were found to be 0.41μm and 0.055μm.

4.2.2 Alignment

An important issue considered in the design of these experiments was alignment. With a droplet height of 25μm and a die dimension of 10mm, alignment of the droplets and the glass slide the droplets comes into contact with was crucial. An alignment method developed by T. Wiser [30] was used.

The method involved using a bare silicon die and thick, slow curing epoxy. A drop of epoxy was placed on the top surface of the aluminum bracket and a bare silicon die was placed on top. Then, with the plate and glass slide mounted above the bare die, the z-axis stage was raised until the bare die was pressed against the glass slide. The epoxy was able to flow underneath the bare die, allowing the die surface to press evenly against the glass slide. The die was held in contact with the glass slide for 28 hours until the epoxy had fully cured. Droplet array dies were then mounted on the top of the bare die.

4.2.3 Load Cell

The load cell used in the static deformation experiments was manufactured by Futek Advanced Sensor Technology. The model used, L2331, was a 0.2lb or ~90g capacity load cell. The load cell was connected to a digital display, model D501, also made by Futek. The display had a five digit readout with adjustable decimal place and tare button. With typical 12g maximum loadings used in the experiments, milligram

resolution was available with the display. However, due to some vibration noise that could not be damped out by the air table mount, the third decimal place was not consistently reliable. As a result, a hundredth of a gram measurement resolution was used. The uncertainty was assumed to be ±5 milligrams.

4.2.4 Laser Positioning System

A combination of a laser and photo detector was used to measure the relative position of the droplet array. The laser was reflected off a horizontal plane cut into the center of the aluminum bracket mount for the droplet array. The photo detector was positioned on the other side of the apparatus to intercept the reflected laser. The photo detector signal was monitored with a multimeter that displayed a voltage. As the test stand apparatus translated vertically, the reflected laser beam image moved across the photo detector. The relationship between voltage output and position was then calibrated. The multimeter was able to measure voltages with a reliable resolution of 10 millivolts. The assumed uncertainty was ±5 millivolts. The corresponding uncertainty in position and displacement was uniquely calculated from each position calibration curve.

4.2.5 Visualization

Digital images were taken of the droplet arrays and large droplets during deformation. These images were then used to statistically analyze the arrays. The measurement technique relied on a computer imaging program, Scion Image. Scion Image was used to count the number of pixels in a digital photograph along a user-specified length. A micrometer scale bar was used as a calibration standard. Using a photograph of the scale bar, the number of pixels was counted over a 100μm length. A calibration constant with units of pixels/micron was then determined. Care was taken so

that all droplet pictures were taken with the same magnification and resolution settings. As a result, the same calibration constant was sufficient to convert all pixel measurements into lengths in microns. The assumed uncertainty in these measurements was ±5 pixels. The corresponding uncertainty in length is calculated from the calibration constant based on five pixels.

4.3 Dynamic Actuation

The characterization of the droplet array mechanical behavior under dynamic actuation was limited to imaging the droplet arrays before and after actuation. The focus of these experiments was in obtaining qualitative information about the droplet array behavior, particularly droplet adhesion and droplet stability, under cyclic loading. As a result, these experiments did not include force, deflection, or contact area measurements as in the static deformation experiments. The apparatus used for dynamic actuation is shown in **Figure 4.2**.

Of particular interest in dynamic characterization experiments was the effect of droplet array alignment on droplet adhesion and stability. To control array alignment, a high precision, bidirectional tilt stage was introduced into the apparatus. With this tilt stage, optical alignment of the droplet array was possible. Droplet array alignment was accomplished by observing the array through a microscope while the droplets were slowly brought into contact with the glass. When one edge of the array was observed to touch the glass, the array was pulled back and then adjustments were made to the tilt stage in the appropriate direction. The array was then raised again into contact and readjusted as many times as were required until all droplets across the array came into contact with the glass slide at the same time.

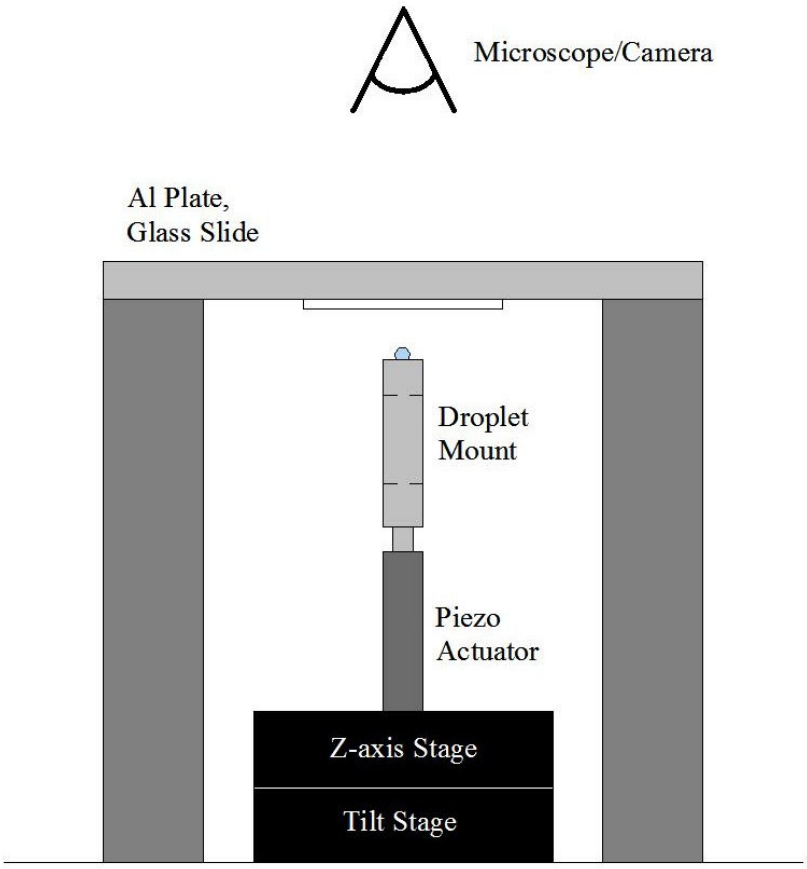

Figure 4.2: Dynamic Actuation Apparatus

It was possible to visually distinguish between droplets in contact and out of contact with the glass slide. The droplet arrays were front lighted using a fiber optic light source. Since the mercury droplets are metallic and spherical, light easily reflected off the droplet surface which was visible in the microscope. When the spherical droplets came into contact with the glass slide and flattened out, the amount of light reflected back to the microscope increased. This increase in reflected light was clearly visible through the microscope.

A piezoelectric actuator driven with an AC voltage signal was used to move the droplet array into and out of contact with the glass slide at specified frequencies over required durations. Images were taken of the droplet arrays with a microscope and digital

camera. A video capture system was used to record video clips of the droplets during dynamic actuation.

4.3.2 Visualization

The video capture system was similar to that used in the static deformation experiments. However, a microscope with a 50x magnification was used to image the droplet arrays. All videos captured were 30s in length and were recorded at the "highest quality" video setting, at a standard video recording speed of 30 frames per second.

4.3.1 Piezoelectric Actuator

The piezoelectric actuator used in the dynamic actuation experiments had an effective operating range of frequencies from 20 to 500 Hz. The maximum amplitude of travel was 30μm. Most actuation experiments were run at 20 Hz for ease of video capturing. However, for high cycle actuation, experiments were run at frequencies of 400 Hz to shorten the duration of the experiment.

CHAPTER 5

EXPERIMENTAL PROCEDURE

5.1 Statistical Analysis

Statistical characterization is used to obtain accurate measures of large populations when measuring and counting large populations is time consuming. For populations with thousands of items, such as a droplet array, it would be time prohibitive to measure and count every droplet of many different arrays. Statistics provide a means for obtaining information about such populations by analyzing a smaller, representative sample from the population. It is important to avoid introducing bias into a gathered sample of data. Careful planning and consistency is required when selecting the representative sample.

For the square grid pattern of the droplet arrays discussed here, organizing and planning the data collection procedure was as follows. The diagonals of the square grid were chosen as the locations of data sampling from the droplet arrays. Any variation in the droplet array distribution was assumed to be grouped together into quadrants. Measuring along the diagonals was assumed to cover all variations of droplet size. Pictures were taken in sequence along each diagonal, using the same magnification. A picture of a scale bar was also taken at the same magnification settings as a reference. Care was taken to not photograph any single droplet more than once. It was important to avoid measuring the same droplet multiple times to avoid potentially biasing the results.

For each photograph, the file was converted into the TIFF format which could be read using the Scion Image program. The scale bar was analyzed to obtain the conversion factor from pixels to microns. Each droplet picture was analyzed to

determine droplet diameters. The data analysis package within Microsoft Excel was used to produce a histogram of the droplet diameters for the sample. The histogram was divided into statistical bins, each covering a diameter range of 2μm. The number of droplets in any bin was defined to be the number of droplets that have diameters between the current bin value and the next lower bin value.

The number of total pictures taken along both diagonals ranged between 8 and 15. Each digital picture contained 20 to 100 droplets each, depending on the magnification and field of view. The time required to measure all of the droplets would be great, so representative samples were chosen.

To calculate a reasonable sample size, three parameters must be known: 1) the 100(1-α)% confidence interval which identifies the **z** value from the standard normal distribution, 2) the population standard deviation σ which can be approximated from the sample standard deviation, and 3) the uncertainty **E** which is chosen. Once these values are known, the sample size is calculated by [32]:

$$n = \frac{(z_{\alpha/2})^2(\sigma)^2}{E^2} \qquad 5.1$$

A 99% confidence interval was chosen, and thus α is equal to 0.01. From a standard normal distribution table, $\mathbf{Z_{\alpha/2}}$ is equal to 2.58. A sample standard deviation of 3μm was initially used to approximate the population standard deviation. The population standard deviation for one array was later measured to be 3.47μm. The uncertainty **E** was chosen to be ±0.5μm. Inserting these values into **Equation 5.1** produces a sample size of 239. This is a minimum required sample size that must be taken to obtain 99% confidence for the mean droplet size with an uncertainty of ±0.5μm.

For accurate statistical sampling, it is important to avoid creating any biases in the data. Droplets were measured at even intervals across each picture, in the same manner for all pictures. Typically, one droplet was skipped between each droplet measured, or alternate rows would be measured instead to reduce the time required. Satellite droplets were also counted and measured if their position was nearer to the target position than other adjacent positions.

The average droplet diameter and standard deviation were calculated for the sample. The number of excess satellite droplets was obtained by subtracting the number of droplets found by the planned number of droplets. If an array were perfect, there would be a droplet on every gold pad and no droplets anywhere else. However, most arrays have extra droplets deposited on the substrate. These extra droplets were counted. A corresponding population for the entire droplet array was extrapolated by comparing the number of droplets counted with the number of targets. In this way, an actual population size was approximated.

Tolerance intervals were calculated to obtain a range of the expected array population based on the sampled data. To obtain this tolerance interval the sample standard deviation **s**, the sample population average **x**, and the factor $\mathbf{C_T}$ must be known. This factor states that a certain percentage **B** of the global population is included in a sample of determined size **n** with a given level of confidence level **W**. The interval is then calculated by [35]:

$$TI = x \pm s * \left(C_{T(B)(W)n}\right) \qquad 5.2$$

5.2 Static Deformation

Both single large droplets of ~200μm diameters and 1600 droplet arrays with 30μm diameter droplets were statically deformed using similar procedures. The first step for both experiments was to clean the glass slide, to ensure all particulates and organic films were removed from the glass. To do this, the glass slide was removed from the aluminum plate and cleaned using a five step cleaning process. Only gloved hands touched the edges of the glass slide after cleaning.

Once cleaned, the glass slide was centered and fixed over the visualization slot in the aluminum plate. Next, the bare silicon base die was glued to the aluminum mounting bracket to achieve good alignment [30]. When the epoxy had cured, the air table was pressurized. The laser was positioned in alignment with the photo detector, and the laser warmed up for 1 hour prior to taking data. The photo detector multimeter was turned on and the voltage output checked. The fiber optic light was positioned for optimal lighting. The visualization system was aligned and focused.

To calibrate the position measurement using the laser photo detector system, metal shims of known thickness were used. First, the position of the bare die against the glass slide was recorded. Next, metal shims of different known thicknesses were placed between the bare die and glass slide, and position measurements for each thickness were recorded. A force of 90g was applied to the metal shims to ensure complete contact. The thickness of the metal shims was correlated to the voltage measurements to obtain a straight line calibration slope. Distances in microns were then calculated from the voltage reading of the photo detector during subsequent measurement.

The z-axis stage was retracted and the top plate removed. A droplet array die was then placed on the base alignment die and the top plate was replaced. For large droplets, a picture was taken of the droplet before contact to obtain the original droplet diameter. For droplet arrays, the droplet diameter distribution was found via statistical characterization prior to testing. After the load cell was zeroed out, the droplet array was slowly brought into contact with the glass slide. The initial contact position was obtained by observing the array through the microscope as the z-stage was raised. When the first sign of contact was observed, the position voltage and load cell reading were recorded. If a large droplet was being studied, a picture was also taken using the digital camera. The z-axis stage was then raised a small amount. Force and position measurements were recorded and pictures were also taken. This same process continued until the force applied was greater than 10g or 0.1 N.

The initial contact point was recorded as the zero deflection point. All subsequent changes in position were taken as deflection. For the large droplets, each picture taken was analyzed to yield contact diameter and contact area. Measurements were plotted in terms of force versus deflection, force versus contact diameter or contact area, and contact diameter versus deflection. For the large droplets, deformed droplet height (original height minus deflection) was plotted against contact diameter. Both deformed droplet height and contact diameter were normalized by the original droplet diameter.

5.3 Dynamic Actuation

In preparation for the dynamic actuation experiments, the z-axis stage was fully retracted and the top plate was removed. The droplet array was fixed to the top surface of the mounting bracket with double sided adhesive. The top plate was replaced and the

array was aligned using the tilt stage and visual monitoring. The droplet array was slowly brought into slight contact with the glass slide. If one portion of the array was in contact while another portion was not, the z-axis stage was lowered and the tilt stage was adjusted accordingly. This was repeated until the entire droplet array came into contact simultaneously.

Once array alignment was established, the z-axis stage was retracted a few hundred microns. The function generator was set to generate a sine wave with the desired operating frequency. The signal was checked by an oscilloscope. The sine wave was then fed into the actuator amplifier and the actuator. The z-axis stage was then slowly raised until a blinking effect could be seen as the droplet array came into and out of contact with the glass slide. By further raising the z-axis stage, the blinking effect could be made to disappear as soon as the droplets were continually in contact with the glass slide. The z-axis stage was set to ensure that the array was actuated into and out of contact with the glass slide. The droplet array behavior was then observed for different numbers of cycles. Short, thirty second video clips were recorded to visually monitor the droplet array behavior during actuation.

CHAPTER 6

RESULTS

6.1 Overview

Results characterizing the mechanical behavior of mercury micro droplet arrays are presented. First, results of the statistical characterization of droplet diameter and array size are given. Second, measurements of force, deflection, and contact diameter from static deformation experiments are discussed. Third, the results of dynamic actuation experiments performed to observe the dynamic response to cyclically actuated droplet arrays are presented. Finally, the results of the thermal model in terms of thermal resistance are compared to measurements reported by T. Wiser [30].

6.2 Statistical Characterization of Droplet Arrays

Three droplet arrays used to experimentally measure thermal resistance were statistically characterized. Both the droplet diameter distribution and the array size, or total number of droplets, were studied.

6.2.1 Droplet Diameter

A histogram of sampled droplet diameters for a 1600 droplet array on die 884H, is shown in **Figure 6.1**. Die 884H was used for experimentally measuring thermal resistance in an air environment at atmospheric pressure [30]. The average droplet diameter of this array was 26.4μm and the standard deviation was 4.35μm. Die 884K was used for experimentally measuring thermal resistance in a xenon environment at atmospheric pressure. The histogram of sampled droplet diameters for die 884K is shown in **Figure 6.2**. The average droplet diameter was measured to be 28.9μm with a standard deviation of 4.9μm.

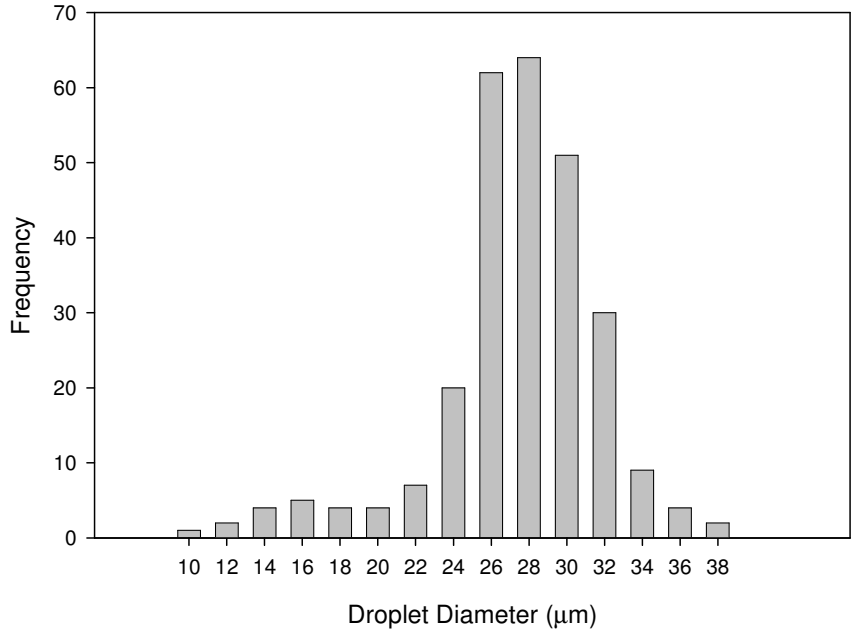

Figure 6.1: Die 884H Air Droplet Diameter Histogram

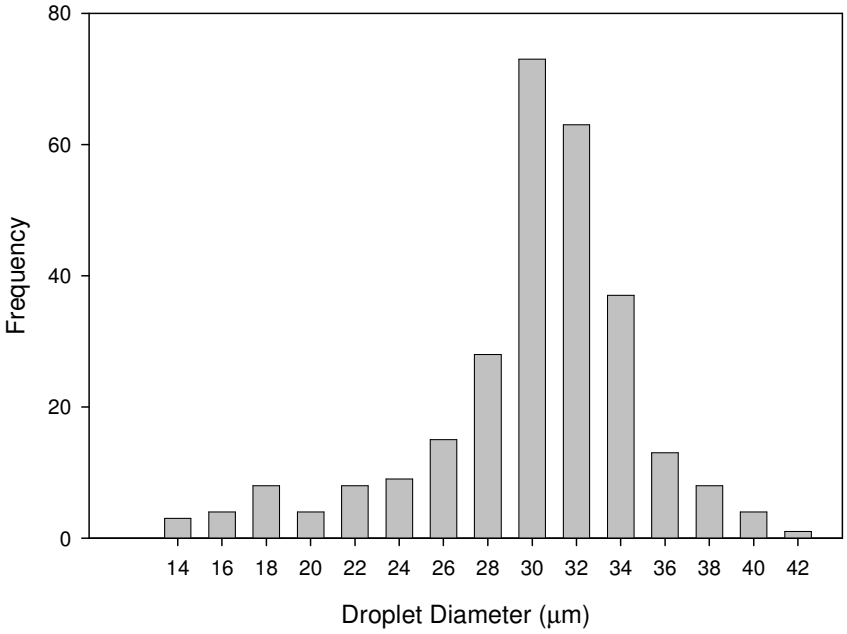

Figure 6.2: Die 884K Xenon Droplet Diameter Histogram

A third die, 964O, was used to experimentally measure thermal resistance in a 0.5 torr vacuum environment. The histogram of sampled droplet diameters for die 964O is shown in **Figure 6.3**. The average droplet diameter measured was 29.9µm and the standard deviation was 7.3µm.

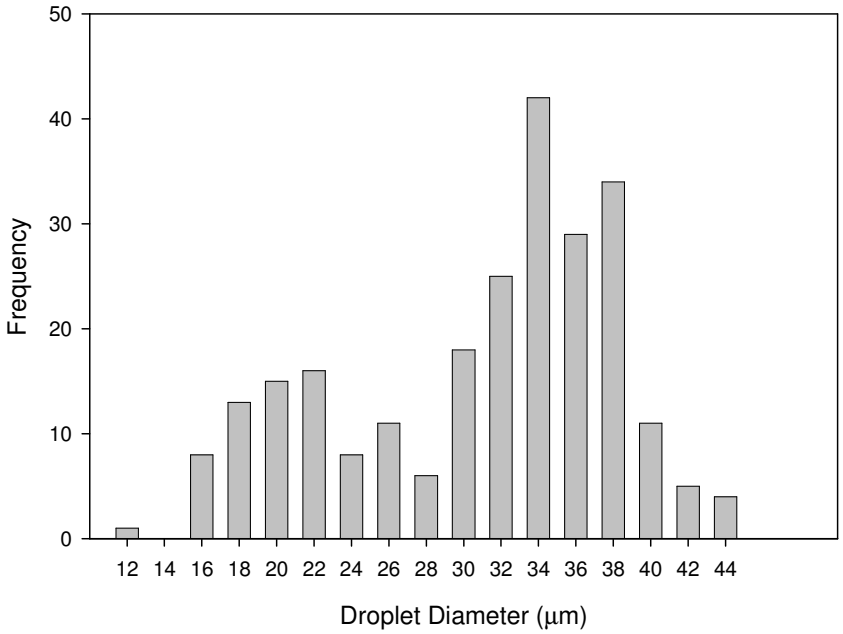

Figure 6.3: Die 964O Vacuum Droplet Diameter Histogram

6.2.2 Array Size

An example of a droplet picture used to produce the histograms shown above is shown in **Figure 6.4**. From the population of excess satellite droplets and total sample population determined from the droplet array images such as that in **Figure 6.4**, a ratio or percentage was calculated for the amount of excess droplets sampled. This ratio was used to predict the total array droplet population. The array size for the die shown in **Figure 6.1** was calculated to be 1537, with a confidence interval of ±278. The array size for **Figure 6.2** was calculated to be 1589±64. The array size for **Figure 6.3** was calculated to be 1406 ±499. All calculations for the confidence interval were made based on a 95% confidence level.

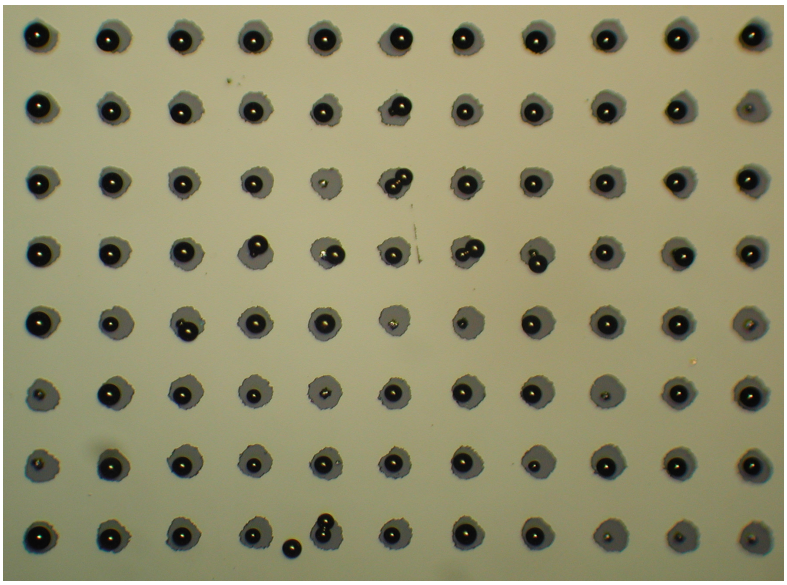

Figure 6.4: Portion of 1600 Droplet Array

6.3 Static Deformation

Results of the mechanical characterization of droplet arrays subjected to a static compressive force between two parallel plates (including the force applied under static loading conditions and the resulting increase in deflection and contact diameter) are presented. Initial contact diameter and deformation hysteresis are discussed first. The results of the coupled force, deflection, and contact diameter measurements are shown and used to validate the mechanical model. The results of the thermal model are compared to experimental measurements obtained from a guard heated calorimeter apparatus [30].

6.3.1 Initial Contact Behavior

The initial contact behavior of a single large droplet is shown in **Table 6.1**. The ratio of initial contact diameter $\mathbf{D_i}$ to original droplet diameter $\mathbf{D_o}$, was used to characterize the initial contact behavior of a droplet. From **Equation 3.4**, inserting $\mathbf{D_o}$ in for **d**, the initial contact diameter $\mathbf{D_i}$ can be calculated. As seen in the table, these values

were measured for a variety of large droplets, all varying in size. The comparison with model predictions is also shown. The experimental ratios varied between 0.29 and 0.42. The model predicted a ratio of 0.43.

Die	Contact Diameter	Outside Diameter	Di/Do Ratio
BD2	145.0	388.0	0.37
BD3a	100.1	291.3	0.34
BD3b	94.4	292.5	0.32
BD4c	112.2	265.0	0.42
BD4d	102.2	270.1	0.38
BD5	56.1	196.8	0.29
BD7	103.4	275.5	0.38
BD8	78.7	186.7	0.42
		Average	0.37
		Standard Deviation	0.05
Model	12.8	30.0	0.43

Table 6.1: Initial Contact Behavior Di/Do Ratio

6.3.2 Deformation Hysteresis

Hysteresis in the deformation behavior was investigated for a large droplet with a diameter of 270μm. Results are shown in **Figure 6.5**. Negative deflections are apparent in the figure, which indicate the droplet remained adhered to the glass slide in a state of tension. As seen in the figure, the droplet was pulled by the glass slide for almost 10μm before it broke contact and returned to its initial spherical shape. Subsequent attempts to come back into contact with the droplet resulted in different initial contact diameters and starting positions, as indicated in the figure. Contact diameters and starting positions shown in the figure for subsequent initial contacts varied between 10 and 20μm from the original value. These measurement variations are small compared to the original droplet size.

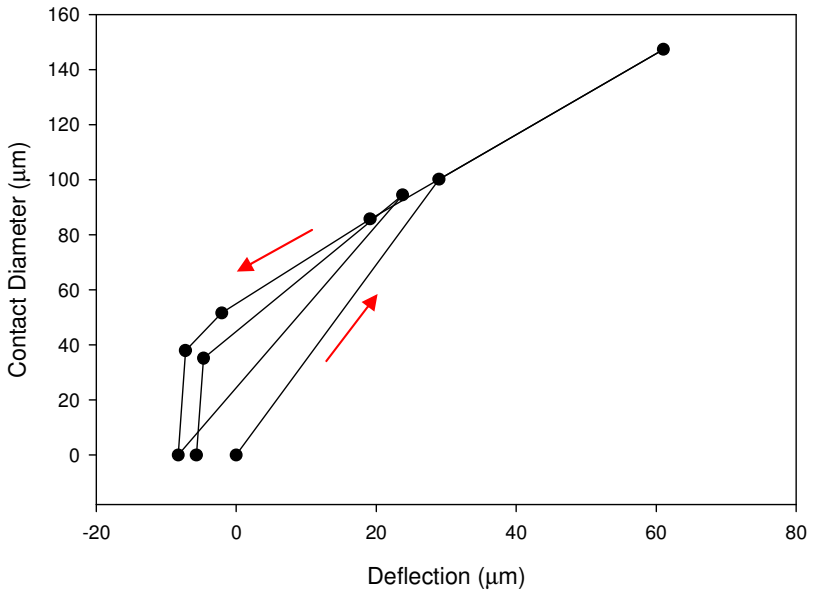

Figure 6.5: Large Droplet Contact Hysteresis

6.3.3 Model Validation

Measurements of force, displacement, and contact diameter were obtained for a large droplet with an original diameter of 197µm and a corresponding height of 174µm. The difference in diameter and height is due to the truncation of the liquid sphere as it sits on the substrate surface.

6.3.3.1 Geometrical Relationship

Figure 6.6 shows measurements of contact diameter and deflection for the large (197 µm dia.) droplet. For comparison, results of the model are also indicated with a solid line. The data are presented in dimensionless form by dividing the measurements of the deflection and the contact diameter by the original droplet size. The data show good agreement with the model.

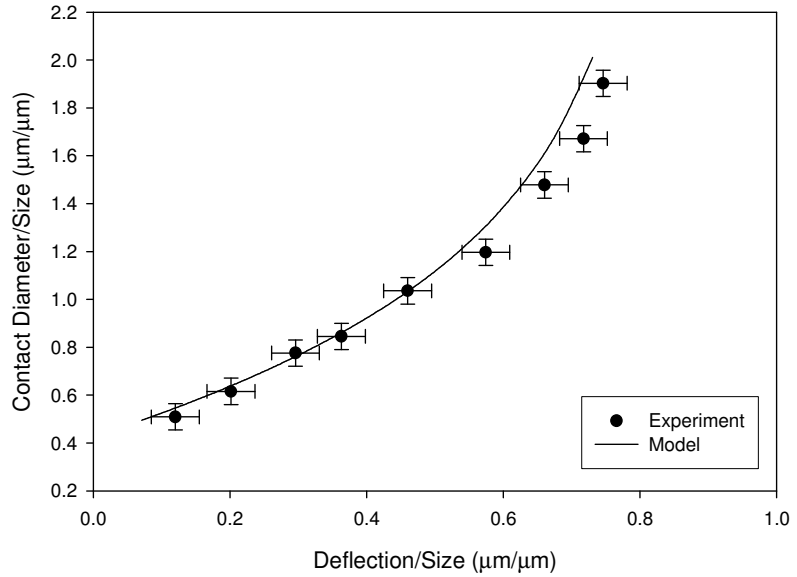

Figure 6.6: Geometric Model Validation

6.3.3.2 Force vs. Deflection

The compliance of the test stand was characterized to ensure accurate measurements of droplet deflection. **Figure 6.7** shows the compliance characterization.

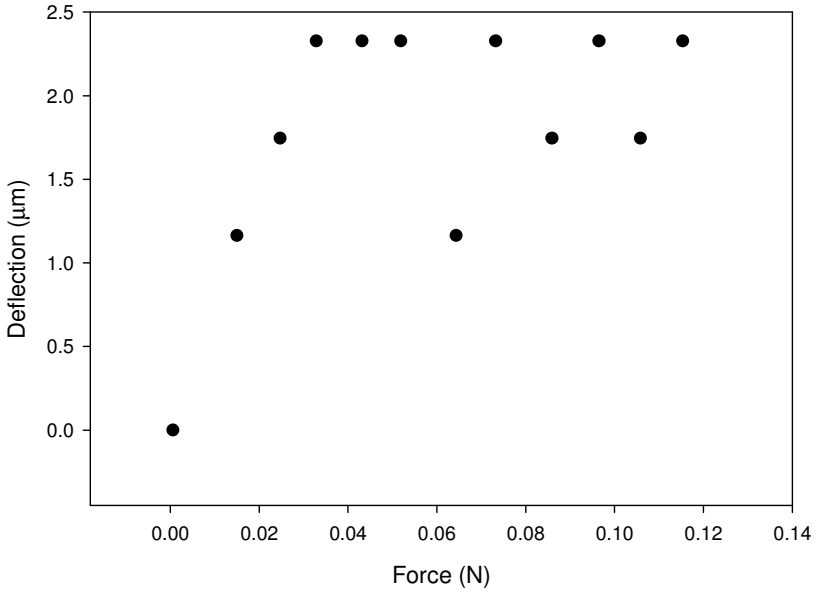

Figure 6.7: Test Stand Compliance

The figure shows that the measured deflection oscillated between 1 and 2.5µm.

This deflection corresponds to less than 10% of the droplet height of a 30µm droplet.

Measurements of force versus deflection results for the large droplet are shown in **Figure 6.8**. Results of the force versus deflection model are shown with a solid line on the same plot.

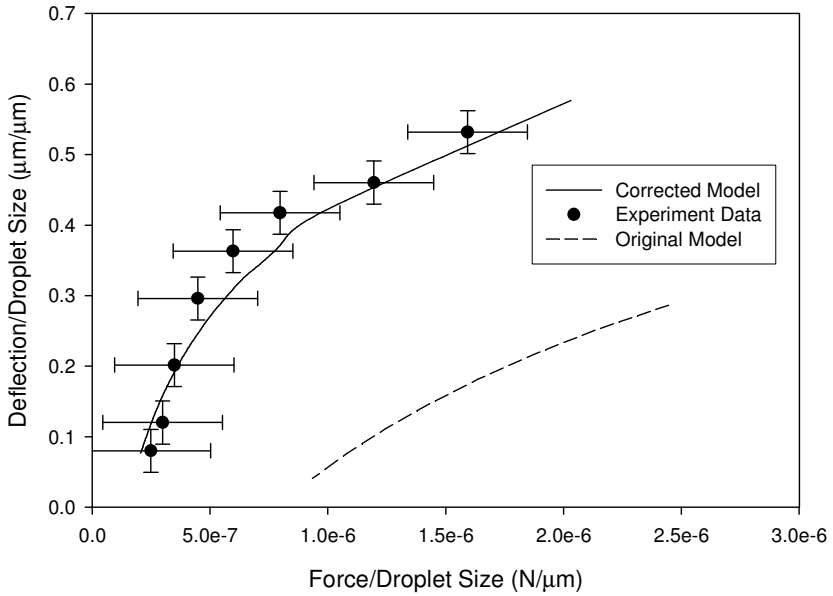

Figure 6.8: Force Deflection Validation

The data were normalized with respect to droplet size. The model and experimental data show good agreement over the range of deflection. Also shown is a dashed line that represents the force versus deflection model prior to including a correction factor in the force data. The correction was included because the model of force versus deflection is a logarithmic function which can never reach zero force. However, in the experiment, zero force is obviously recorded. Based on the initial contact study, when the droplet makes initial contact with the glass slide, the droplet seems to "jump" into contact with the glass slide. An initial contact area is present, even though no discernable force has been applied to deform the droplet. Other factors must be at work to influence this behavior and lend a degree of complication to the problem which this model does not fully

describe. D. Packham [36] reports in his paper that this behavior can be explained by surface tension and adhesion forces.

Another argument includes remembering the fact that the force is obtained by calculating the capillary pressure of the liquid inside the droplet and multiplying by the contact area. This assumption fails for the model near zero force. Even when the plate is not in contact, there is still an absolute pressure inside the droplet. Fortunately, the exact behavior of this relationship at very small forces does not severely impact the behavior of the droplet as it is deformed at higher loads. This low force behavior was ignored.

6.3.3.3 Thermal Resistance vs. Force

The parameter study shown in **Table 6.2** was performed to characterize the behavior of the droplet array thermal resistance by changing physical parameters of the droplet array.

Droplet Radius Effects (Held Array Size Constant)

	Droplet Radius (um)	Max Thermal Resistance (K/W)	Min Thermal Resistance (K/W) at 0.1 N	Difference (K/W)
Smaller Droplet	14	11.412	8.111	3.30
Baseline	15	8.713	6.264	2.45
Larger Droplet	16	6.793	4.933	1.86

Array Size Effects (Held Droplet Radius Constant)

	Array Size	Max Thermal Resistance (K/W)	Min Thermal Resistance (K/W) at 0.1 N	Difference (K/W)
Smaller Array	1493	9.261	6.667	2.59
Baseline	1600	8.713	6.264	2.45
Larger Array	1707	8.227	5.906	2.32

Table 6.2: Parameter Study

Changing the droplet radius from 15μm to 16μm is a 6.3% change. The modeled thermal resistance changed by 22% (from 8.71 to 6.79). A similar 6.3% change in the array size (from 1600 to 1707) changed the thermal resistance by 5.6% (from 8.71 to 8.22). Clearly the droplet diameter is the parameter of most influence in the model.

The thermal model calculations were compared with experimental measurements of thermal resistance taken from T. Wiser [30]. The experimental data of die 884H in an air environment at atmospheric pressure are shown in **Figure 6.9**. A thermal conductivity of 0.0263 W/mK was used in the air model.

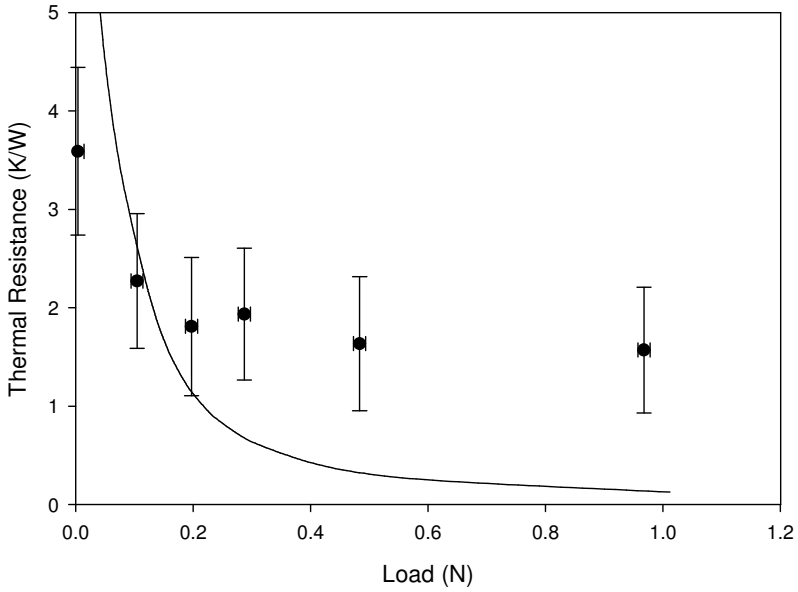

Figure 6.9: Thermal Resistance Comparison in Air

The air model is shown as a solid line. **Figure 6.10** shows the model compared with experimental results of die 884K in a xenon environment at atmospheric pressure. A thermal conductivity of 0.00565 W/mK was used in the xenon model. The xenon model is shown as a solid line. Experimental results for die 964O in a 0.5 torr air vacuum are shown in **Figure 6.11**. A small discrepancy between the experiments and the model is apparent. A thermal conductivity of 0.00623 W/mK was used in the vacuum model. The vacuum model is shown as a solid line.

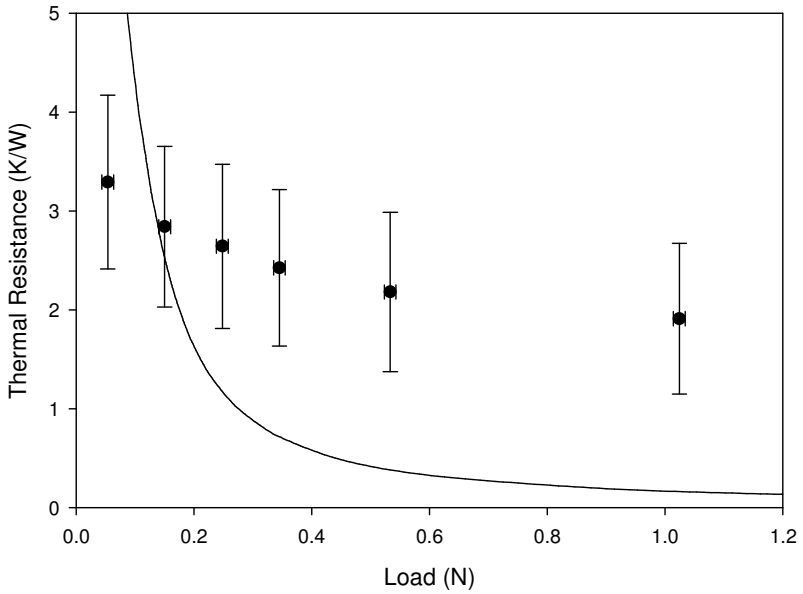

Figure 6.10: Thermal Resistance Comparison in Xenon

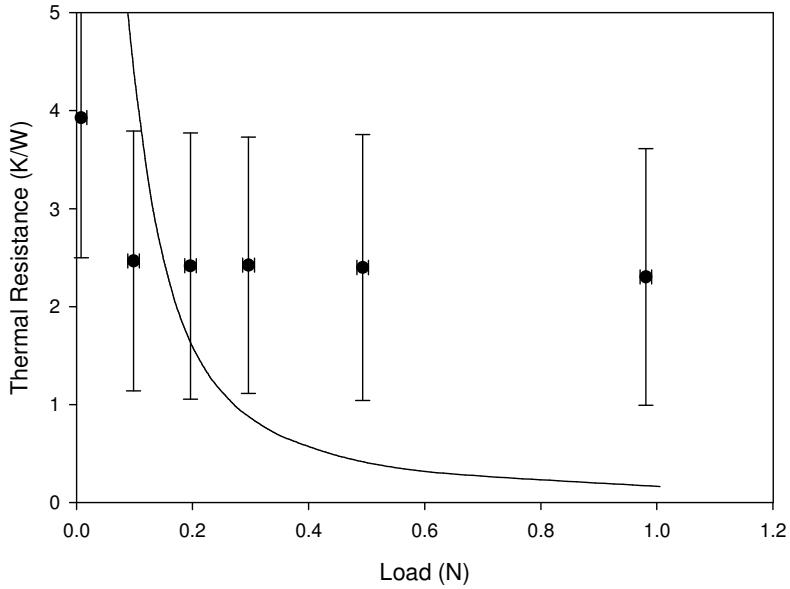

Figure 6.11: Thermal Resistance Comparison in Vacuum

The experimental results for both the vacuum and xenon environments show large increases in thermal resistance. The model, in comparison, shows much smaller increases, especially at high forces. At low forces, the model for vacuum and xenon predicts a y-axis intersection at much larger thermal resistances as compared to air at

atmospheric conditions. This follows what would be expected, since xenon and vacuum have much lower thermal conductivities. However, the axis scales have been adjusted for clarity at lower thermal resistances, so this intersection is not shown. The model does not predict the results of the experiment very well. There is suspicion of experimental bias in these results, which may explain the discrepancies.

Additionally, the model was calculated for each die in each gas environment. Three plots, one for each die, are shown in **Figures 6.12**, **6.13**, and **6.14**. Each plot shows the comparison of thermal resistance of a single droplet distribution in air, vacuum, and xenon gas environments.

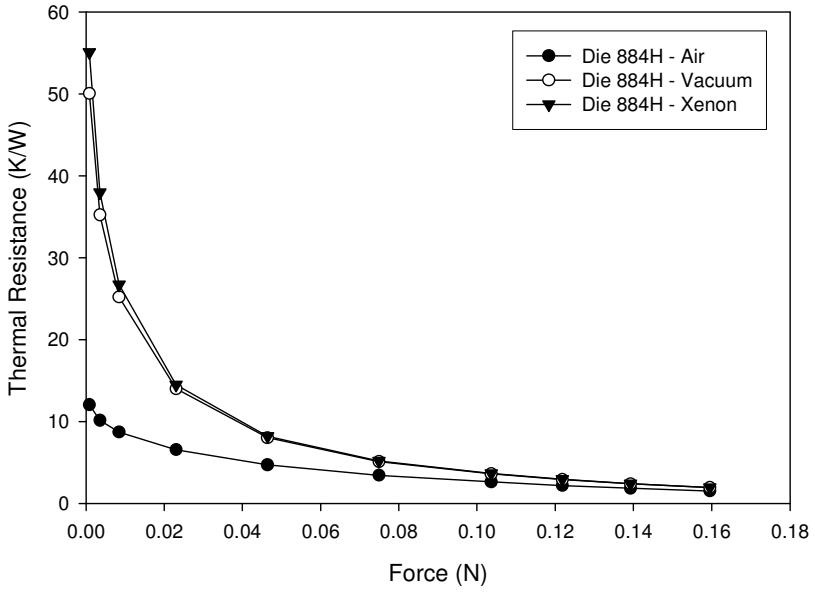

Figure 6.12: Modeled Thermal Resistance for Die 884H

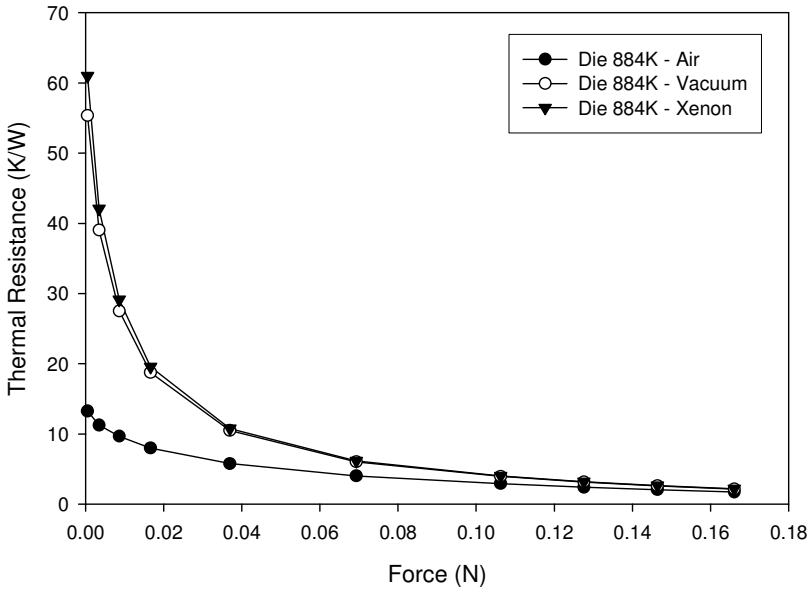

Figure 6.13: Modeled Thermal Resistance for Die 884K

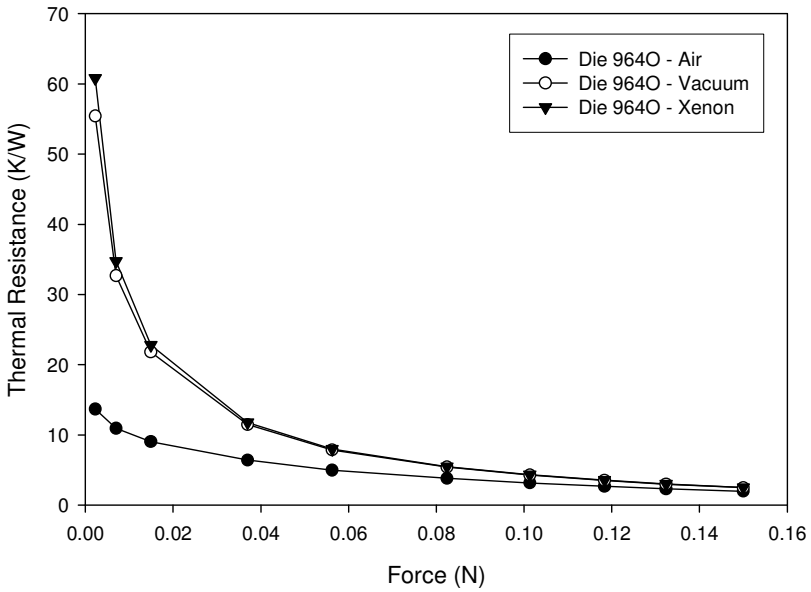

Figure 6.14: Modeled Thermal Resistance for Die 964O

6.4 Dynamic Actuation

Droplet arrays were dynamically actuated repeatedly in and out of contact with a glass slide, and the array behavior was observed. This test simulated conditions that would be similar to the cyclic switch operation expected with the P3 micro heat engine.

6.4.1 Droplet Stability

Figure 6.12 shows a droplet array that was actuated 10,000 times. This array was deposited without a photoresist protection layer and with the silicon dioxide layer exposed.

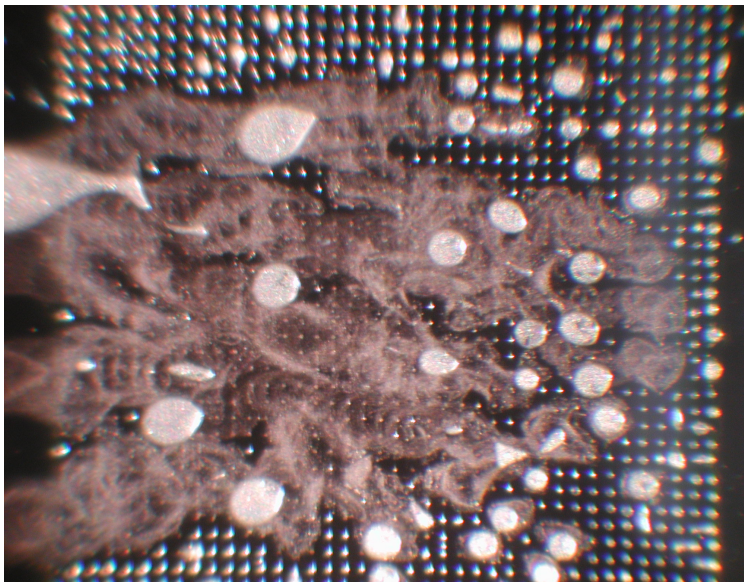

Figure 6.15: Droplet Array Deterioration during Actuation

When the array was actuated, the droplets were seen to translate across the oxide substrate surface with relative ease and cause severe array deterioration.

Figure 6.13 shows a picture of a droplet array, deposited with a 2μm photoresist layer over the silicon dioxide layer, after actuation for 30 minutes at a frequency of 20 Hz or 36,000 cycles. The droplets are still in contact with the glass slide.

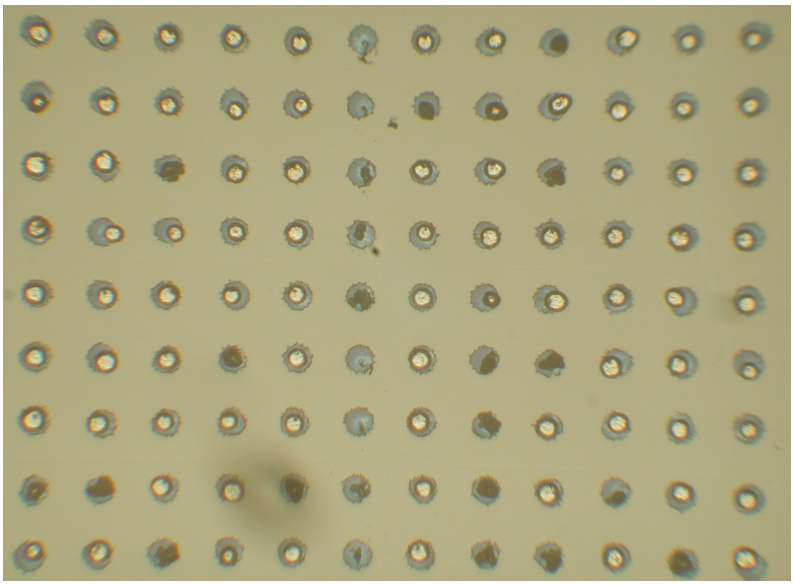

Figure 6.16: 10,000 Cycle Actuation

The droplets are seen to have remained stably anchored to the gold pad positions in the array. There was no visible deterioration of the array. These same results were observed by actuating a similar droplet array for 90 minutes at 20 Hz, which corresponds to over 100,000 cycles, shown in **Figure 6.14**.

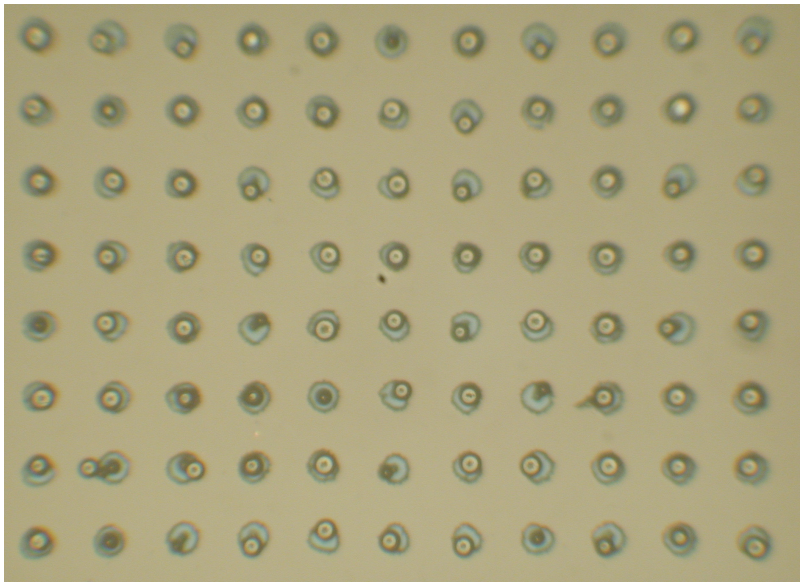

Figure 6.17: 100,000 Cycle Actuation

A final actuation experiment involved a droplet array run at 400 Hz for 45 minutes, which equals over a million cycles in and out of contact with the glass slide. This is shown in **Figure 6.15**. The droplets are in contact with the glass slide.

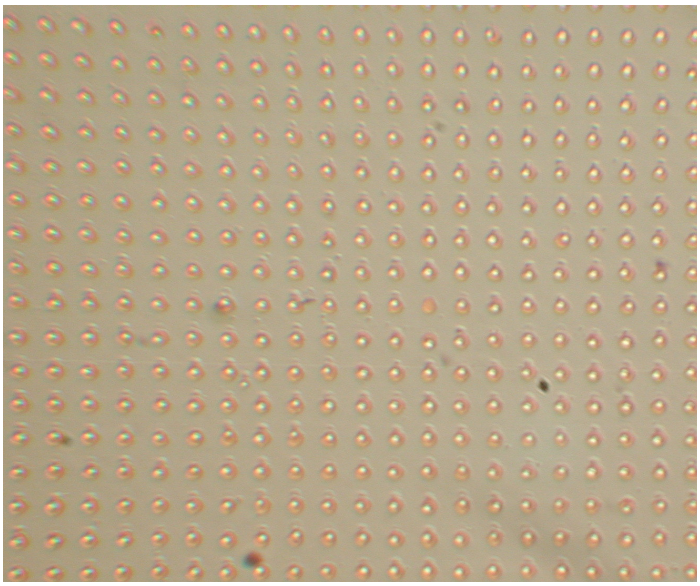

Figure 6.18: Million Cycle Actuation

6.4.2 Optical Alignment

Alignment of the array with the glass slide was investigated. An array with a misalignment of 0.6° was actuated at a frequency of 20Hz for 30 minutes. **Figure 6.16** shows the results. As can be seen in the image taken towards the end of actuation, the droplets remained stable and the array was unaffected.

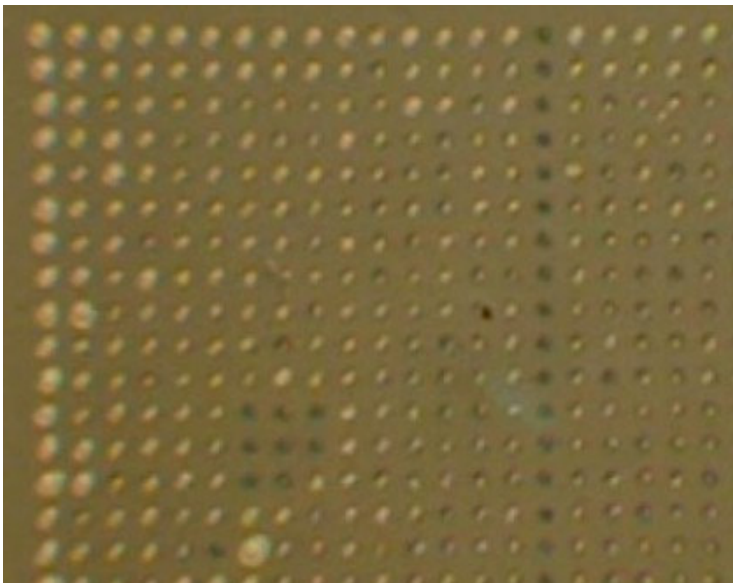

Figure 6.19: Misaligned Actuation

CHAPTER 7

CONCLUSIONS

7.1 Static Deformation

Droplet behavior under static deformation has been studied and characterized. A geometric model of the relationship between deflection and contact diameter was derived and validated by visualizing droplets during deformation. The deflection of a deformed droplet squeezed between parallel plates with given force was modeled and compared with experimental results. The comparison showed good correlation between the model and the experimental measurements. The model predicted the experimental data within the error bars given to the data.

7.2 Dynamic Actuation

Dynamic droplet array behavior was also characterized by actuating droplet arrays into contact with a glass. Droplet arrays were visually observed actuating over ten thousand, one hundred thousand, and one million cycles with the glass slide. Results showed no array deterioration during the span of the tests. The droplets remained anchored and stable under aligned conditions and conditions where the plates were misaligned by 0.6°. The use of a photoresist protection layer has proven to be successful in reducing droplet array deterioration over extended actuation.

7.3 Thermal Model

Thermal resistance was calculated for a droplet array under a range of applied loads. The thermal resistance of a 1600 droplet array ranged from 12 K/W at zero load to 0.12 K/W at a load of 1N in an atmospheric air environment. The average diameter of the droplets was assumed to be 26μm. The size distribution was taken to be that which was statistically characterized for an actual array tested experimentally. The actual array

size was calculated to be 1537. By introducing an alternative gas environment, such as xenon at atmospheric pressure, the thermal resistance ranged from over 60 K/W at zero load to 0.15 K/W at a load of 1N for a 1600 array. For the droplet array tested in the xenon environment, the average diameter of droplets was assumed to be 29μm, and the actual array size was assumed to be 1589. For the droplet array tested in the 0.5 torr vacuum environment, the average diameter of the droplets was assumed to be 30μm, and the actual array size was assumed to be 1406. The thermal resistance also ranged from 60 K/W at zero load to 0.16 K/W at a load of 1N in vacuum.

The thermal model did not compare well with the experimental measurements of thermal resistance. In air, the experimental value of thermal resistance at a force of 1N was 0.38 K/W. In xenon, the thermal resistance was measured to be 1.9 K/W. In vacuum, the experimental value of thermal resistance was 2.2 K/W.

APPENDIX

The following is the derivation of geometric relationship. The volume of the outlined region shown in **Figure A.1**, when revolved around the x-axis, is defined as $V = \int_0^d \pi[f(x)]^2 dx$ where f(x) is a circular arc segment of the circle defined by a radius R_2, with its center located at (d/2, a-b).

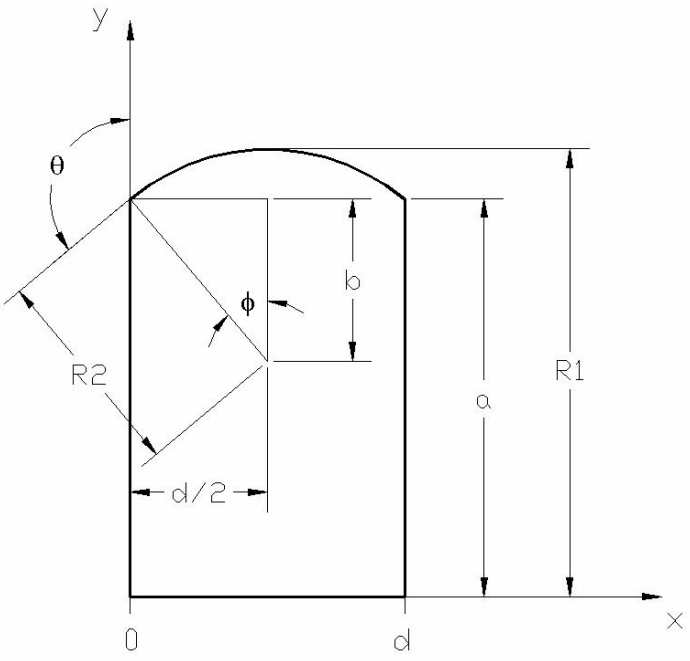

Figure A.1: Two Dimensional, Axisymmetric Representation of Deformed Droplet

The definition of the circle is $R_2^2 = (x-m)^2 + (y-n)^2$ where $m = d/2$ and $n = a - b$. By analyzing the geometry, $b = \frac{d}{2\tan\phi}$ and $R_2 = \frac{d}{2\sin\phi}$. Accepting that r is perpendicular to the tangent of the circle at (0,a), then $\phi = 90 - [180 - \theta]$. θ is given to be 130° which is a material property. Thus, $\phi = 40° = \frac{2\pi}{9}\ radians$. A solution is sought of the form $a = a(d, \phi, V)$.

First, the equation for f(x) is obtained from the equation of a circle. Relevant geometric parameters are obtained from **Figure A.1**.

$$r^2 = (x-m)^2 + (y-n)^2$$
$$(y-n)^2 = r^2 - (x-m)^2$$
$$y = \sqrt{r^2 - (x-m)^2} + n$$
$$f(x) = y = \sqrt{\left(\frac{d}{2\sin\phi}\right)^2 - \left(x - \frac{d}{2}\right)^2} + \left(a - \frac{d}{2\tan\phi}\right)$$

Next, f(x) is inserted into the equation for volume of the revolved region. This is then reduced to a series of integrals.

$$V = \int_0^d \pi \left[\sqrt{\left(\frac{d}{2\sin\phi}\right)^2 - \left(x - \frac{d}{2}\right)^2} + \left(a - \frac{d}{2\tan\phi}\right)\right]^2 dx$$
$$\frac{V}{\pi} = \int_0^d \left[\sqrt{\left(\frac{d}{2\sin\phi}\right)^2 - \left(x - \frac{d}{2}\right)^2} + \left(a - \frac{d}{2\tan\phi}\right)\right]\left[\sqrt{\left(\frac{d}{2\sin\phi}\right)^2 - \left(x - \frac{d}{2}\right)^2} + \left(a - \frac{d}{2\tan\phi}\right)\right] dx$$
$$\frac{V}{\pi} = \int_0^d \left[\left(\frac{d}{2\sin\phi}\right)^2 - \left(x - \frac{d}{2}\right)^2 + \left(a - \frac{d}{2\tan\phi}\right)^2 + 2\left(a - \frac{d}{2\tan\phi}\right)\sqrt{\left(\frac{d}{2\sin\phi}\right)^2 - \left(x - \frac{d}{2}\right)^2}\right] dx$$
$$\frac{V}{\pi} = \int_0^d \left(\frac{d}{2\sin\phi}\right)^2 dx - \int_0^d \left(x - \frac{d}{2}\right)^2 dx + \int_0^d \left(a - \frac{d}{2\tan\phi}\right)^2 dx + 2\left(a - \frac{d}{2\tan\phi}\right)\int_0^d \sqrt{\left(\frac{d}{2\sin\phi}\right)^2 - \left(x - \frac{d}{2}\right)^2}\, dx$$

Each integral is then evaluated.

$$\int_0^d \left(\frac{d}{2\sin\phi}\right)^2 dx = \left(\frac{d}{2\sin\phi}\right)^2 \int_0^d dx = d\left(\frac{d}{2\sin\phi}\right)^2 = \frac{d^3}{4\sin^2\phi}$$
$$\int_0^d \left(x - \frac{d}{2}\right)^2 dx = \int_0^d \left(x^2 - xd + \frac{d^2}{4}\right) dx = \int_0^d x^2 dx - d\int_0^d x\, dx + \frac{d^2}{4}\int_0^d dx = \frac{d^3}{3} - \frac{d^3}{2} + \frac{d^3}{4} = \frac{d^3}{12}$$
$$\int_0^d \left(a - \frac{d}{2\tan\phi}\right)^2 dx = \left(a - \frac{d}{2\tan\phi}\right)^2 \int_0^d dx = d\left(a - \frac{d}{2\tan\phi}\right)^2 = d\left(a^2 - \frac{ad}{\tan\phi} + \frac{d^2}{4\tan^2\phi}\right)$$
$$= a^2 d - \frac{ad^2}{\tan\phi} + \frac{d^2}{4\tan^2\phi}$$

$$\int_0^d \sqrt{\left(\frac{d}{2\sin\phi}\right)^2 - \left(x-\frac{d}{2}\right)^2}\,dx = \int_{-d/2}^{d/2} \sqrt{A^2-u^2}\,du = \frac{1}{2}\left[u\sqrt{A^2-u^2} + A^2\sin^{-1}\left(\frac{u}{A}\right)\right]\Bigg|_{d/2}^{-d/2}$$

where $u = x-\frac{d}{2},\ du = dx,\ A = \frac{d}{2\sin\phi}$

$$\sin^{-1}\left(\frac{d}{2A}\right) = \sin^{-1}\left(\frac{d}{2}\frac{2\sin\phi}{d}\right) = \sin^{-1}(\sin(\phi)) = \phi = \frac{2\pi}{9}$$

$$\frac{1}{2}\left[u\sqrt{A^2-u^2} + A^2\sin^{-1}\left(\frac{u}{A}\right)\right]\Bigg|_{d/2}^{-d/2} = \frac{1}{2}\left[\frac{d}{2}\sqrt{A^2-\frac{d^2}{4}} + A^2\sin^{-1}\left(\frac{d}{2A}\right)\right] + \frac{1}{2}\left[\frac{d}{2}\sqrt{A^2-\frac{d^2}{4}} - A^2\sin^{-1}\left(\frac{-d}{2A}\right)\right]$$

$$= \frac{d}{4}\sqrt{\frac{d^2}{4\sin^2\phi}-\frac{d^2}{4}} + \frac{d^2}{8\sin^2\phi}\frac{2\pi}{9} + \frac{d}{4}\sqrt{\frac{d^2}{4\sin^2\phi}-\frac{d^2}{4}} + \frac{d^2}{8\sin^2\phi}\frac{2\pi}{9}$$

$$= \frac{d}{2}\sqrt{\frac{d^2}{4\sin^2\phi}-\frac{d^2\sin^2\phi}{4\sin^2\phi}} + \frac{\pi d^2}{18\sin^2\phi}$$

$$= \frac{d}{2}\sqrt{\frac{d^2}{4\sin^2\phi}(1-\sin^2\phi)} + \frac{\pi d^2}{18\sin^2\phi} \text{ and we know that } 1-\sin^2\phi = \cos^2\phi$$

$$= \frac{d}{2}\sqrt{\frac{d^2}{4\tan^2\phi}} + \frac{\pi d^2}{18\sin^2\phi} = \frac{d^2}{4\tan\phi} + \frac{\pi d^2}{18\sin^2\phi}$$

The four terms are then inserted back into the equation for V and the equation is simplified.

$$\frac{V}{\pi} = \frac{d^3}{4\sin^2\phi} - \frac{d^3}{12} + a^2 d - \frac{ad^2}{\tan\phi} + \frac{d^3}{4\tan^2\phi} + 2\left(a-\frac{d}{2\tan\phi}\right)\left(\frac{d^2}{4\tan\phi} + \frac{\pi d^2}{18\sin^2\phi}\right)$$

$$\frac{V}{\pi} = \frac{d^3}{4\sin^2\phi} - \frac{d^3}{12} + a^2 d - \frac{ad^2}{\tan\phi} + \frac{d^3}{4\tan^2\phi} + \frac{ad^2}{2\tan\phi} + \frac{ad^2\pi}{9\sin^2\phi} - \frac{d^3}{4\tan^2\phi} - \frac{d^3\pi\cos\phi}{18\sin^3\phi}$$

$$\frac{V}{\pi} = a^2 d - \frac{ad^2}{\tan\phi} + \frac{ad^2}{2\tan\phi} + \frac{ad^2\pi}{9\sin^2\phi} + \left(\frac{d^3}{4\sin^2\phi} - \frac{d^3}{12} - \frac{d^3\pi\cos\phi}{18\sin^3\phi}\right)$$

The equation is then rearranged into the form of a quadratic polynomial. Then, the quadratic formula is used to solve for the contact radius **a**.

$$0 = a^2(d) + a\left(\frac{d^2\pi}{9\sin^2\phi} - \frac{d^2}{2\tan\phi}\right) + \left(\frac{d^3}{4\sin^2\phi} - \frac{d^3}{12} - \frac{d^3\pi\cos\phi}{18\sin^3\phi} - \frac{V}{\pi}\right)$$

$$a = \frac{-B \pm \sqrt{B^2-4AC}}{2A}$$

The equation is then algebraically simplified into the final form.

$$a=\frac{-\left(\frac{d^2\pi}{9\sin^2\phi}-\frac{d^2}{2\tan\phi}\right)\pm\sqrt{\left(\frac{d^2\pi}{9\sin^2\phi}-\frac{d^2}{2\tan\phi}\right)\left(\frac{d^2\pi}{9\sin^2\phi}-\frac{d^2}{2\tan\phi}\right)-4d\left(\frac{d^3}{4\sin^2\phi}-\frac{d^3}{12}-\frac{d^3\pi\cos\phi}{18\sin^3\phi}-\frac{V}{\pi}\right)}}{2d}$$

$$a=-\frac{1}{2d}\left(\frac{d^2\pi}{9\sin^2\phi}-\frac{d^2}{2\tan\phi}\right)\pm\frac{1}{2d}\sqrt{\frac{d^4\pi^2}{81\sin^4\phi}-\frac{d^4\pi}{9\sin^2\phi\tan\phi}+\frac{d^4}{4\tan^2\phi}-\frac{4d^4}{4\tan^2\phi}+\frac{4d^4}{12}+\frac{4d^4\pi\cos\phi}{18\sin^3\phi}+\frac{4dV}{\pi}}$$

$$\frac{1}{2d}=\sqrt{\frac{1}{4d^2}}$$

$$a=\frac{d}{4\tan\phi}-\frac{d\pi}{18\sin^2\phi}\pm\sqrt{\frac{d^2\pi^2}{324\sin^4\phi}-\frac{d^2\pi\cos\phi}{36\sin^2\phi\sin\phi}+\frac{d^2}{16\tan^2\phi}-\frac{d^2}{4\sin^2\phi}+\frac{d^2}{12}+\frac{d^2\pi\cos\phi}{18\sin^3\phi}+\frac{V}{d\pi}}$$

$$a=\frac{d\cot\phi}{4}-\frac{d\pi}{18\sin^2\phi}\pm\sqrt{\frac{V}{d\pi}+\frac{d^2\pi^2}{324\sin^4\phi}+\frac{d^2\pi\cos\phi}{36\sin^3\phi}+\left(\frac{d^2\cos^2\phi}{16\sin^2\phi}-\frac{d^2}{4\sin^2\phi}+\frac{d^2}{12}\right)}$$

$$\left(\frac{d^2\cos^2\phi}{16\sin^2\phi}-\frac{d^2}{4\sin^2\phi}+\frac{d^2}{12}\right)=\frac{d^2\left(1-\sin^2\phi\right)}{16\sin^2\phi}-\frac{d^2}{4\sin^2\phi}+\frac{d^2\sin^2\phi}{12\sin^2\phi}$$

$$\left(\frac{d^2\cos^2\phi}{16\sin^2\phi}-\frac{d^2}{4\sin^2\phi}+\frac{d^2}{12}\right)=\frac{3d^2}{48\sin^2\phi}-\frac{3d^2\sin^2\phi}{48\sin^2\phi}-\frac{12d^2}{48\sin^2\phi}+\frac{4d^2\sin^2\phi}{48\sin^2\phi}$$

$$\left(\frac{d^2\cos^2\phi}{16\sin^2\phi}-\frac{d^2}{4\sin^2\phi}+\frac{d^2}{12}\right)=-\frac{8d^2}{48\sin^2\phi}-\frac{d^2}{48\sin^2\phi}+\frac{d^2\sin^2\phi}{12\sin^2\phi}$$

$$\left(\frac{d^2\cos^2\phi}{16\sin^2\phi}-\frac{d^2}{4\sin^2\phi}+\frac{d^2}{12}\right)=-\frac{d^2}{6\sin^2\phi}-\frac{d^2(1-\sin^2\phi)}{48\sin^2\phi}=-\frac{d^2\cot^2\phi}{48}-\frac{d^2}{6\sin^2\phi}$$

$$a=\frac{d\cot\phi}{4}-\frac{d\pi}{18\sin^2\phi}\pm\sqrt{\frac{V}{d\pi}+\frac{d^2\pi^2}{324\sin^4\phi}+\frac{d^2\pi\cos\phi}{36\sin^3\phi}-\frac{d^2\cot^2\phi}{48}-\frac{d^2}{6\sin^2\phi}}$$

REFERENCES

1 C.D. Richards, D.F. Bahr, R.F. Richards, "A Micro Heat Engine for MEMS Power", *American Society of Mechanical Engineers, Fluids Engineering Division (Publication) FED* **258**, 501-509 (2002).

2 S. Whalen, M. Thompson, et al, "Design, Fabrication, and Testing of the P^3 Micro Heat Engine", *Sensors and Actuators A:Physical*, **104,** n3, 290-298 (2002).

3 T. Nast, G. Bell, C. Barnes, "Development of Gas Gap Cryogenic Thermal Switch", Lockheed Palo Alto Research Laboratories, 1117-1124.

4 F. H. Milanez, M. B. H. Mantelli, "Theoretical and Experimental Studies of a Bi-Metallic Heat Switch for Space Applications", *International Journal of Heat and Mass Transfer* **46**, 4573-4586 (2003).

5 M. A. Beasley, et al, "MEMS Thermal Switch for Spacecraft Thermal Control", *Proceedings of SPIE* **5344**, 98-105 (2004).

6 T. Slater, et al, "Thermomechanical Characteristics of a Thermal Switch", *Sensors and Actuators A* **53**, 423-427 (1996).

7 P. C. Ho, R. B. Hallock, "A Compact Design for an Indium Heat Switch", *Journal of Low Temperature Physics* **121**, 797-802 (2000).

8 H. L. Wang, T. Wagner, G. Eska, "An Aluminum Heat Switch Made From Cold-Pressed Cu-Al Composite", *Physica B* **284-288**, 2024-2025 (2000).

9 P. R. Roach, et al, "Mechanically Operated Thermal Switches for Use at Ultralow Temperatures", *American Institute of Physics* **46**, 207-209 (1975).

10 C. Hilbert, et al, "Thermoelectric MEMS Coolers", *18th International Conference on Thermoelectrics*, 117-122 (1999).

11 K. Shen, X. Chen, M. Guo, J. Cheng, "A Microchip-Based PCR Device Using Flexible Printed Circuit Technology", *Sensors and Actuators B* **105**, 251-258 (2005).

12 Internet Source: P. R. Roach, "A ^{3}He-Gap Heat Switch for Use Below 2K in Zero G", http://irtek.arc.nasa.gov/cryogroup/archive/PR91CEC.

13 J. Yamamoto, M. Yanai, "Precooling of a Superconducting Magnet Using a Cryocooler and Thermal Switches", *American Institute of Physics* **50**, 1382-1385 (1979).

14 J. P. Torre, G. Chanin, "Heat Switch for Liquid-Helium Temperatures", *American Institute of Physics* **55**, 213-215 (1984).

15 V. V. Rau, K. Bapurao, J. Nagaraju, M. V. K. Murthy, "Instrumentation to Measure Thermal Contact Resistance", *Institute of Physics Measurement Science and Technology* **15**, 275-278 (2004).

16 H. Fujishiro, T. Okamoto, K. Hirose, "Thermal Contact Resistance Between High-T_c Superconductor and Copper", *Physica C* **357-360**, 785-788 (2001).

17 A. Lahmar, et al, "Experimental Investigation on the Thermal Contact Resistance Between Gold Coating and Ceramic Substrates", *Thin Solid Films* **389**, 167-172 (2001).

18 E. G. Wolff, D. A. Schneider, "Prediction of Thermal Contact Resistance Between Polished Surfaces", *International Journal of Heat and Mass Transfer* **41**, 3469-3482 (1998).

19 M. Antler, "Gold Plated Contacts: Effect of Thermal Aging on Contact Resistance", *IEEE*, 121-131 (1997).

20 M. G. Burzo, P. L. Komarov, P. E. Raad, "Non-Contact Thermal Conductivity Measurements of P-Doped and N-Doped Gold Covered Natural and Isotopically-Pure Silicon and their Oxides", *5th International Conference on Thermal and Mechanical Simulation and Experiments in Micro-Electronics and Micro-Systems,* 269-276 (2004).

21 J. L. Sample, K. J. Rebello, H. Saffarian, R. Osiander, "Carbon Nanotube Coatings for Thermal Control", *IEEE Inter Society Conference on Thermal Phenomena*, 297-301 (2004).

22 R. S. Prasher, J. C. Matayabas, "Thermal Contact Resistance of Cured Gel Polymeric Thermal Interface Material", *IEEE Transactions on Components and Packaging Technologies* **27**, 702-709 (2004).

23 C. P. Chiu, G. L. Solbrekken, Y. D. Chung, "Thermal Modeling of Grease-Type Interface Material in PPGA Application", *13th IEEE Semi-Therm Symposium*, 57-63 (1997).

24 A. O. Christensen, et al, "Fabrication and Characterization of a Liquid Metal Micro-Droplet Array for Use as a Thermal Switch", *Proceedings ASME heat Transfer Conference*, (2003).

25 A. O. Christensen, Fabrication and Characterization of Liquid-Metal Micro-Droplet Thermal Switch, Masters of Science in Mechanical Engineering, Washington State University, USA (2003).

26 W. Shen, J. Kim, "CJ" Kim, Controlling the Adhesion Force for Electrostatic Actuation of Microscale Mercury Drop by Physical Surface Modification, *IEEE*, 52-55 (2002).

27 L. Latorre, "CJ" Kim, et all, Electrostatic Actuation of Microscale Liquid-Metal Droplets, *Journal of MEMS Vol. 11,* **4**, 302-308 (2002).

28 J. N. Simon, A Liquid Filled Microrelay With a Moving Mercury Micro-Drop, PhD Dissertation, University of California Los Angeles (1997).

29 N. K. Adam, The Physics and Chemistry of Surfaces, Dover Publications Inc., New York, 8-10 (1968).

30 T. Wiser, Steady State Heat Transfer Characterization of a Liquid Metal Thermal Switch, Masters of Science in Mechanical Engineering, Washington State University, USA (2005).

31 C. T. Crowe, et al, Engineering Fluid Mechanics, 7th edition, John Wiley, New York, A-13 (2001).

32 R. L. Ott, M. Longnecker, An Introduction to Statistical Methods and Data Analysis, 5th edition, Duxbury, Pacific Grove, 110 (2001).

33 F. P. Incropera, D. P. DeWitt, Introduction to Heat Transfer, 4th edition, John Wiley, New York, 837 (2002).

34 R. C. Hibbeler, Mechanics of Materials, 4th edition, Prentice Hall, New Jersey, 800 (2000).

35 H. W. Coleman, W. G. Steele, Experimentation and Uncertainty Analysis for Engineers, 2nd edition, John Wiley, New York, 16-34 (1999).

36 D.E. Packham, Work of Adhesion: Contact Angles and Contact Mechanics, *Int. J. Adhesion and Adhesives Vol. 16 No. 2,* **16,** 121-128 (1996).